Photoacoustic Spectroscopy

David Birtill[1], Anant Shah[1,2], Michael Jaeger[1,2], Andreas Gertsch[1], Jeffrey Bamber[1]
[1]Joint Department of Physics, [2]CRUK-EPSRC Cancer Imaging Centre, Institute of Cancer Research and Royal Marsden NHS Foundation Trust, Downs Road, Sutton, Surrey, SM2 5PT

***Abstract*—A photoacoustic (PA) spectroscopy system has been built to study the differences between the PA spectra of oxygenated and deoxygenated blood, and various PA contrast agents, with a view to optimising the identification of these media in clinical PA images. A variable-wavelength laser delivers short (ns) pulses of light, via a fibre optic cable, into a sample held between 75 μm transparent membranes. The optical wavelength is controlled by a computer, which scans the wavelength range 400-700 nm using a different pulse for each wavelength. Each pulse causes the sample to momentarily expand and emit a pressure wave, the energy of which is measured by the computer using a digital oscilloscope that samples the signal from a strongly focused 7.5 MHz ultrasound transducer. The resulting optical spectra are corrected for some system variables, such as the wavelength-dependent laser energy. Further corrections are planned, so that the measurement is truly of optical absorption coefficient at each wavelength. Even without these additional corrections however, the measured PA spectrum of oxygenated blood strongly resembles the published optical absorption spectrum.**

These results suggest that, in addition to its intended use for determining the optimum wavelengths for clinical PA imaging of blood oxygenation level and contrast agent concentration, this system may have applications as a laboratory spectrophotometer. Unlike traditional transmission spectrophotometers, which measure the extinction coefficient, the PA spectrometer will measure the absorption coefficient. This will make it suitable for use with (a) optically dark samples such as normal blood, which cannot be analysed in a standard spectrophotometer without dilution, and (b) turbid media, which normally require an optical scatter-correction to convert the extinction coefficient to an absorption coefficient.

***Index Terms*—Photoacoustic spectroscopy, photoacoustic imaging, optoacoustic imaging, blood spectrum, optical absorption.**

Introduction

Photoacoustic Imaging (PAI) inspects the optical absorption of the tissue. Tissue is irradiated using short laser pulses and ultrasound waves are generated within the tissue upon optical absorption (Wang 2009, Lai and Young 1982, Sigrist and Kneubuhl 1972, Jaeger 2007). An image is formed of the optical contrast based on the arrival times of the acoustic waves. As blood has a high optical absorption over much of the optical spectrum, photoacoustics can be used to detect blood vessels and could be used to determine the cancer's stage, as advanced tumours create their own blood vessel network to sustain the tumour. Photoacoustics can be taken further by changing the wavelength of the emitted laser pulse. An image acquired at different wavelengths enables spatially resolved spectrometry. Therefore it should be possible to separate signals from oxygenated blood and deoxygenated blood to determine hypoxia. Hypoxia is important in oncology as it has been shown to be associated with tumour aggressiveness, angiogenesis and local recurrence; it affects and is affected by radiation therapy and some chemotherapy agents (Tatum at al. 2006, Semenza et al. 2007, Vaupel and Mayer 2007).

A photoacoustic (PA) spectroscopy system has been built to study the differences between the PA spectra of oxygenated and deoxygenated blood, and various PA contrast agents, with a view to optimising the identification of these media in clinical PA images.

Method

This system comprises of a multiwavelength OPO (Optical Parametric Oscillator) laser system (Continuum Powerlite plus Panther OPO) which emits a laser pulse at a given wavelength. This light is guided by a fibre optic cable into the water bath, directed at a thin box with two 75 μm optically transparent membranes 2mm apart (Opticell) filled with 10ml of human venous blood (figure 1a). Then the emitted photoacoustic wave is detected by a focused 7.5 MHz single element ultrasound transducer. The acoustic signal was recorded by an oscilloscope using the laser Q-switch trigger for starting the acquisition. For each illuminating wavelength 100 traces were averaged to reduce noise. Then a low pass filter was used to reduce high frequency noise (figure 1b). The peak to peak amplitude was recorded over the visible wavelength range of 420 nm to 700 nm with a step size of 10 nm, shown in figure 2b. Also the energy of the laser output at the fibre optic cable exit was measured 100 times for each illuminating wavelength to produce a plot of the mean energy spectrum with the standard error as shown in figure 2a. The relative absorption coefficient for venous blood, calculated by dividing the peak to peak amplitude by the illuminating energy for each wavelength, is shown in figure 2c. This relative absorption coefficient μ_a^* assumes the following relation:

$$\mu_a^*(\lambda) = \frac{V(\lambda)}{E(\lambda)} = \mu_a(\lambda)\Gamma K$$

where V is the signal amplitude (voltage), E is the energy of the laser output both of which are wavelength (λ) dependent. Before the true optical absorption coefficient μ_a can be calculated the other system dependent variable K, which includes the transducers response to the intensity of the acoustic wave, and the Gruneisen coefficient Γ, which is a combination of the thermal expansion coefficient, sound speed, and specific heat capacity of the sample medium, needs to be known and accounted for (Soroushian 2010). As the Gruneisen coefficient is not wavelength dependent and to first order does not vary greatly between water based samples, this small variation is neglected at this stage. The other system dependent

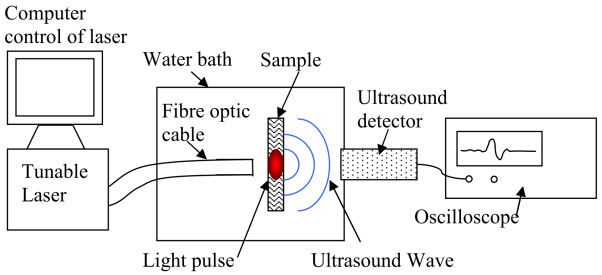

(a) Diagram of the photoacoustic setup

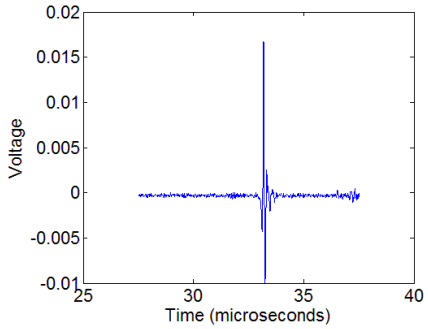

(b) Photoacoustic signal after noised suppression using a low pass filter.

Figure 1: Diagram of the photoacoustic setup with photoacoustic signal

variable K is assumed to be wavelength independent when the scattering is much larger than the absorption, therefore for this wavelength range it is neglected at this stage.

Results and Discussion

The photoacoustically obtained spectrum of venous blood (about 75% oxygenated) is compared to the known spectrum of oxy- and deoxy-hemoglobin in figure 3a. The photoacoustic relative absorption coefficient has an arbitrary unit and not the same as the optical absorption coefficient. The shape of the photoacoustic spectrum shares several features with oxy-hemoglobin which nicely demonstrates that multiwavelength photoacoustics can be used to measure the photoacoustic spectrum of blood. Also an experiment using the same method on two test objects of blue and red tape, producing the relative absorption coefficient of the two objects, as shown in figure 3b, demonstrate that the method can distinguish between different objects. Although the shape of the relative absorption coefficient of the venous blood is generally comparable there are issues with the method which still need to be resolved. Neglecting the change in units, the shape of the spectrum of venous blood when compared to known values does change slightly. It is hypothesised that the majority of the light is being absorbed in a thin layer of the blood at lower wavelengths (400-450nm) due to the very high absorption in this range. This would result in not much variation in the photoacoustic signal amplitude between different wavelengths in this range. Once this method has been tested on blood with varying oxygenation levels it will be possible using the current technique to determine the optimum wavelengths for measuring the blood oxygenation level.

In addition to the proposed (above) experiment the relative absorption spectra of a sample of gold nano-rods and spheres with transverse plasmon resonance at 520nm and longitudinal plasmon resonance of 690nm was measured using the same method. The relative absorption spectrum corresponds closely to that measured using a standard UV spectrophotometer (Jenway), see figure 4. In future this work could be used to photoacoustically characterise the destruction threshold of gold nano rods, which is important if they are to be used as a clinical imaging contrast agent. The laser could be tuned to the Plasmon resonance of the nano rod and the decay of the signal over number of shots for different laser energies could be measured.

These results suggest that, in addition to its intended use for determining the optimum wavelengths for clinical PA imaging of blood oxygenation level and contrast agent concentration, this system, once optimised, may have applications as a laboratory spectrophotometer. Unlike traditional transmission spectrophotometers, which measure the extinction coefficient, the PA spectrometer will measure the absorption coefficient. This will make it suitable for use with (a) optically dark samples such as normal blood, which cannot be analysed in a standard spectrophotometer without dilution, and (b) turbid media, which normally require an optical scatter-correction to convert the extinction coefficient to an absorption coefficient.

Acknowledgements

This work would not have been possible without the funding provided by the Institute of Cancer Research and the laser system loaned from the STFC.

References

[1] Jaeger, M. “Real-time Optoacoustic Imaging for Medical Diagnostics Using Linear Array Transducers”. PhD Thesis University of Bern, 2007.

[2] Lai, H.M. and K. Young. “Theory of the pulsed optoacoustic technique”. *J. Acoust. Soc. Am.* **72** No. 6 (1982): 2000-2007.

[3] Semenza, G.L et al. “Hypoxia and Cancer”. *Cancer and Metastasis Reviews* **26** No. 2 (2007): 223-224.

[4] Sigrist, M.W. and F.K. Kneubuhl. “Laser-generated stress waves in liquids”. *J. Acoust. Soc. Am.* **64** No. 6 (1978): 1652-1663.

[5] Soroushian, B. et. al.“Study of laser-induced thermoelastic deformation of native and coagulated ex-vivo bovine liver tissues for estimating their optical and thermomechanical properties” *J. Biomed Opt.* **15** No. 6 (2010): 065002.

[6] Tatum, J.L. at al. “Hypoxia: Importance in tumor biology, noninvasive measurement by imaging, and value of its measurement in the management of cancer therapy”. *International Journal of Radiation Biology* **82** No. 10 (2006): 699-757.

[7] Vaupel, P. and A. Mayer “Hypoxia in cancer: significance and impact on clinical outcome”. *Cancer and Metastasis Reviews* **26** No. 2 (2007): 225-239.

[8] Wang, L.V. “Photoacoustic Imaging and Spectroscopy”, CRC Press Taylor and Francis Group, Boca Raton, 2009.

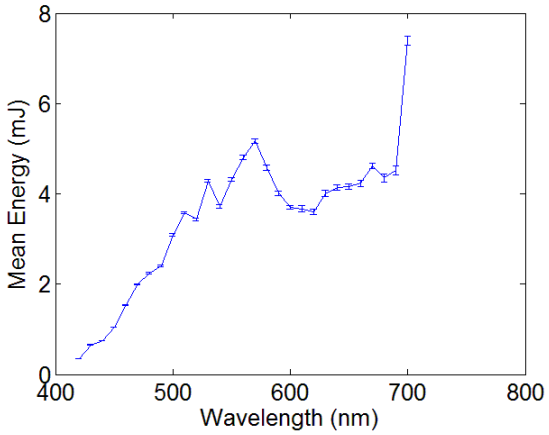

(a) Energy spectrum from output of the fibre optics

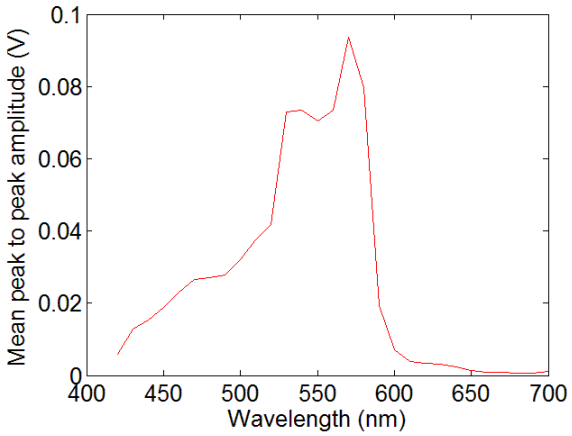

(b) Peak to peak amplitude spectrum for venous blood.

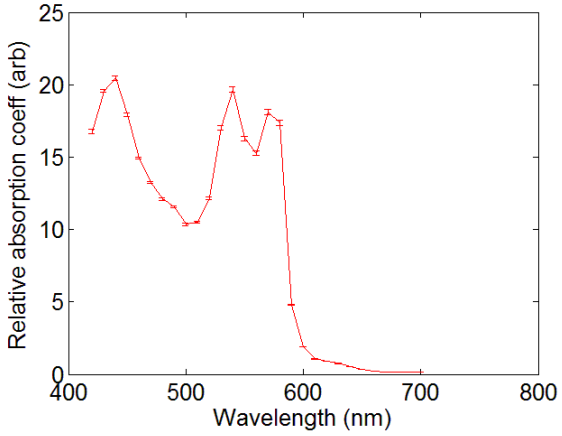

(c) Relative absorption spectrum for blood

Figure 2: The illuminating energy spectrum (a), the photoacoustic peak to peak amplitude spectrum of venous blood(b) and the relative absorption coefficient spectrum of venous blood (c)

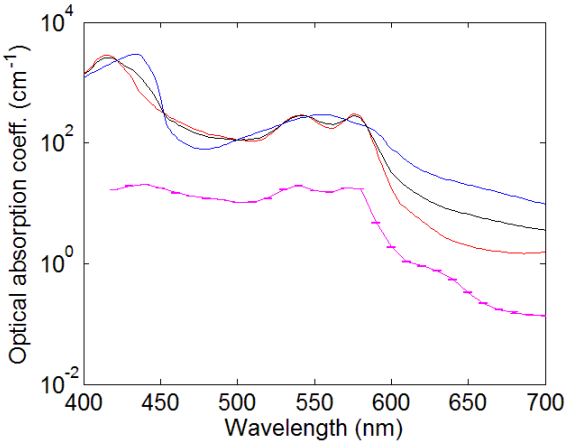

(a) The magenta line is the relative absorption spectra of venous blood measured photoacoustically, note this has an arbitrary unit. Compared to previously established results of the optical absorption coefficient assuming a molar concentration of 150 Hb/litre, red line is oxyhemoglobin (HbO_2), blue line is the deoxyhemoglobin (Hb) and black line corresponds to 75% oxygenated hemoglobin. Data from http://omlc.ogi.edu/spectra/hemoglobin/summary.html.

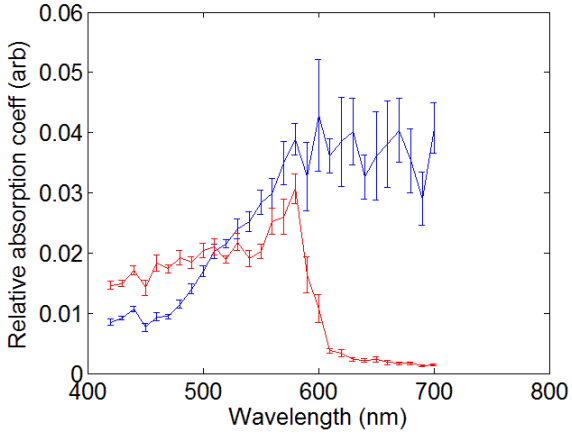

(b) The relative absorption coefficient of two test objects of blue (blue line) and red (red line) electrical tape. Where the error shown is one standard error from the mean.

Figure 3: The relative absorption coefficient of venous blood compared to known optical absorption values of oxy- and deoxy-hemoglobin values (a). The relative absorption coefficient of test objects: blue and red tape (b).

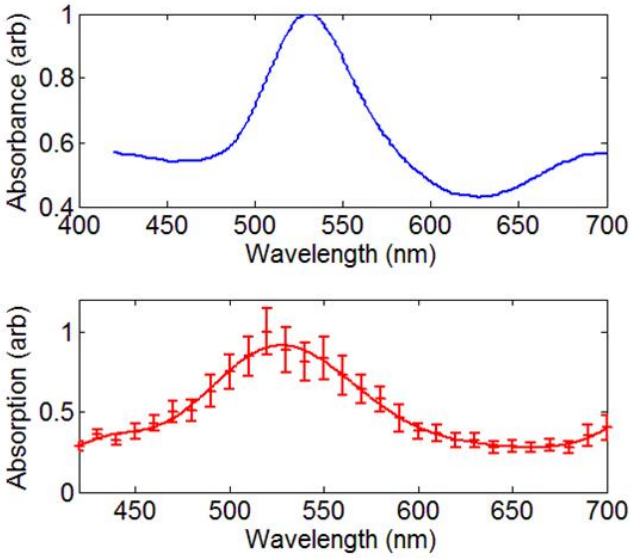

Figure 4: A comparison of spectras of gold nanoparticles using two different methods, absorbance spectrum using a standard spectrophotometer (blue) and photoacoustic relative absorptipon spectrum (red).

Two-Photon Excited Fluorescence Lifetime Imaging of the Intracellular Uptake of (*E*)-Combretastatin Derivatives

Contact *r.h.bisby@salford.ac.uk*

R. H. Bisby, J. A. Hadfield, A. T. McGown, K. M. Scherer

Biomedical Sciences Research Institute
University of Salford
Salford, M5 4WT, UK

S. W. Botchway, A. W. Parker

Research Complex at Harwell Rutherford Appleton Laboratory
STFC
Chilton, Oxfordshire, OX11 0QX, UK

Introduction

This study investigated the intracellular uptake of *E*-combretastatin analogues (Figure 1) into live mammalian cells using multiphoton fluorescence lifetime microscopy (FLIM). Combretastatins, and especially combretastatin A4, have been recognized as powerful anticancer drugs in their *Z*-configuration more than a decade ago. They are small stilbene-like organic molecules that were first extracted from the African bush willow *Combretum caffrum* by Pettit and his co-workers in 1982 [**1**]. A water-soluble phosphate ester derivative of *Z*-Combretastatin A4 is currently in phase II/III clinical trials [**2**].

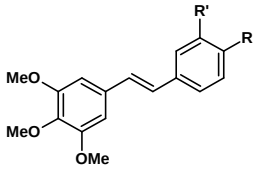

1 R = OMe, R' = OH
2 R = OMe, R' = F
3 R = OMe, R' = NH_2
4 R = $N(CH_3)_2$, R' = H

Figure 1 Molecular structure of *E*-combretastatin derivatives (**1** *E*-CA4, **2** *E*-CA4F, **3** *E*-ACA4 and **4** *E*-DMAC)

Compared with the *Z*-form, the *E*-isomers show ~ 2-3 orders of magnitude lower cytotoxicity towards cancer cells [**3**]. The objective of the project is to investigate the use of *E*-combretastatins as prodrugs which may be converted to the more active *Z*-isomer by photoisomerisation in living tissues. The activated *Z*-isomers act by binding to the colchine binding-site in the β-tubulin subunit, inhibiting tubulin polymerization to microtubules and eventually preventing cell growth and division.

Z-combretastatins are only very weakly fluorescent, but *E*-isomers have appreciable fluorescence (Φ_F 0.05 to 0.40) depending on the solvent and λ_{max} 390 - 450 nm. The use of this fluorescence was investigated as a means to observe combretastatin uptake into living mammalian cells.

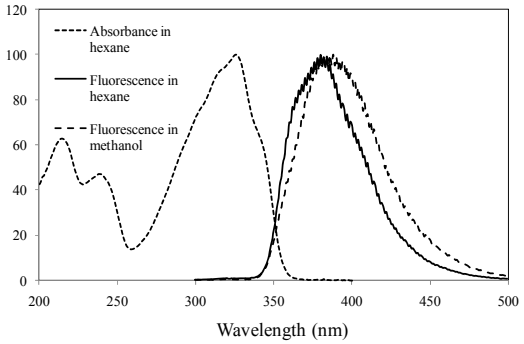

Figure 2 Normalised absorption and fluorescence spectra of *E*-CA4F in hexane and methanol.

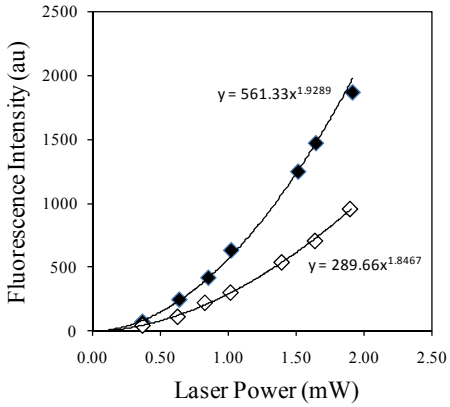

Figure 3 Nonlinear power-dependence of two-photon excited fluorescence from *E*-CA4 (◇) and *E*-ACA4 (◆) (0.5 mM) in dichloromethane excited at 620 nm.

Conventional one-photon excitation requires UV wavelengths (300 – 350 nm) which may be absorbed by chromophores in biological tissues, and therefore prevent photoactivation. It is suggested to overcome this problem by the use of two-photon activation in the near-infrared, as deeper tissues penetration is possible in this wavelength regime [**4**]. High resolution images of the *E*-combretastatins time-resolved uptake into live mammalian cells, and intracellular lifetime distributions were obtained using two-photon excited multiphoton fluorescence lifetime imaging microscopy (FLIM).

Four different *E*-combretastatin derivatives, (*E*)-Combretastatin A4 (*E*-CA4, **1**), a fluorinated (*E*-CA4F, **2**), an amino (*E*-ACA4, **3**) and a dimethylamino analogue (*E*-DMAC, **4**) (Figure 1) were used in the experiments and their uptake into live CHO (Chinese Hamster Ovarian), HeLa (cervical cancer cells) and PC-3 (human prostate cancer) cells was studied.

Results and Discussion

Spectroscopy

The absorption spectrum of *E*-CA4F has a maximum at 326 nm in hexane and a fluorescence maximum at 380 nm in hexane (Figure 2). There is relatively little effect of solvent on the fluorescence with the peak shifting to 388 nm in methanol. We are currently studying other combretastatin derivatives which exhibit larger solvatochromic behavior and which may have larger two photon absorption cross sections. Excitation of *E*-CA4 and other derivatives (Figure 3) with ultrafast laser pulses at 620-630 nm, or approximately half the energy of the one-photon peak, using the system described by Botchway et al [5]. Fluorescence intensities were determined to show quadratic dependence on laser power, confirming a two-photon mechanism. Fluorescence lifetimes were also measured with two-photon excitation at 630 nm and showed strong dependence

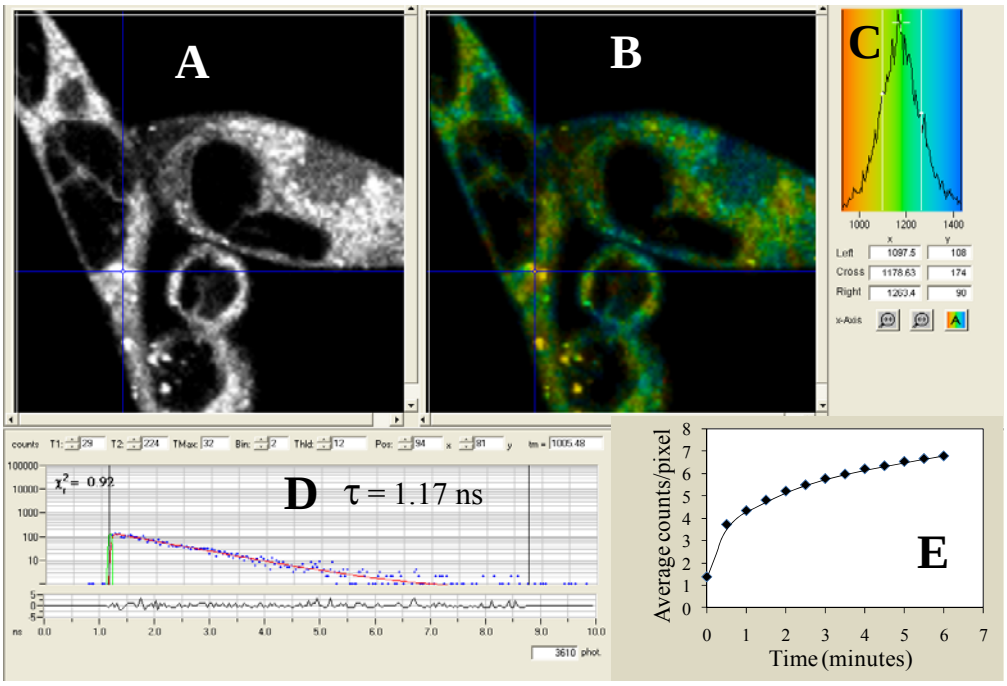

Figure 4 Two-photon fluorescence lifetime imaging of *E*-CA4F in PC-3 cells. The intensity (**A**) and lifetime (**B**) images are show after incubation with *E*-CA4F (10 μM) for 10 minutes. The lifetime distribution (**C**) is shown together with a single pixel fluorescence decay (**D**). The time-dependent increase in intracellular fluorescence intensity after addition of *E*-CA4F to the cells is shown in **E**.

on solvent polarity and viscosity. For E-CA4F lifetimes varied between 440 ps in methanol, 750 ps in hexane and 1,070 ps in glycerol. Such behavior is typical for stilbenes in which fluorescence decay competes with photoisomerisation. Overall it was found that a linear relation existed between fluorescence lifetime and quantum yield and this proved to be extremely valuable in estimating intracellular drug concentrations (see below).

Intracellular uptake of combretastatins

The accumulation of *E*-combretastatins in living prostate cancer PC-3 cells was observed using two-photon excited FLIM. Figure 4A shows a fluorescence intensity image of *E*-CA4F distribution in PC-3 cells measured 10 minutes after addition of the compound. The combretastatin is seen to be excluded from the cell nucleus and to reside within regions of the cytoplasm and some punctuate structures inside the cell. The latter are identified as lipid droplets by co-localisation with nile red (results not shown), a dye that labels lipid droplets and cell membranes [6]. The fluorescence lifetime of *E*-CA4F in the cell (Figure 4 B,C,D) has a distribution centered around 1.18 ns, suggesting that it is located in a viscous environment. This is consistent with the viscosities of cell membranes and triglycerides (the latter a major component of lipid droplets). Figure 4E shows the rate of accumulation of *E*-CA4 into PC-3 cells at room temperature. Uptake appeared to be biphasic with a fast unresolved component followed by slower accumulation over a period of minutes.

Similar results were obtained for accumulation of *E*-CA4 and *E*-CA4F into Chinese hamster ovary (CHO) and HeLa cells. Intracellular concentrations were estimated from fluorescence intensities, adjusted for the quantum yield as deduced from the linear correlation with fluorescence lifetime. Starting with combretastatin concentrations of 10 μM in the surrounding medium, the intracellular concentrations in the cytoplasmic regions were estimated to be up to around 500 μM, whereas lipid droplets were found to containing drug concentrations up to 5 mM. Therefore the intracellular concentration of drug may exceed that in the extracellular medium by 2-3 orders of magnitude.

Conclusions

The results show significant accumulation of combretastatins into live mammalian cells. Further investigations will explore the conversion of intracellular *E*-combretastatins to the more cytotoxic Z-isomer using two-photon activation with ultrafast laser pulses. It is interesting to note that whilst cellular assays of *E*-CA4 toxicity indicate LD_{50}'s in the nanmolar region [2], the true intracellular concentration of the drug may be considerably higher, and closer to micromolar concentrations at which tubulin aggregation is affected [7].

Acknowledgements

We would like to thank the STFC for a Biomed Network studentship to KMS and the University of Salford for financial support. We also acknowledge the help of Dr Rahul Yadav with the subculture of cells at LSF and Dr Nicholas Hirst for his help with the synthesis of candidate compounds.

References

1. Pettit, G.R., Singh, S.B., Boyd, M.R., Hamel, E., Pettit, R.K., Schmidt, J.M., Hogan, F. (1995) Antineoplastic Agents. 291. Isolation and Synthesis of Combretastatins A4, A5, and A6. *J. Med. Chem.*, **38**: 1666 – 1672.

2. Hadfield, J.A., Ducki, S., Hirst, N., McGown, A.T. (2003) Tubulin and microtubules as targets for anticancer drugs. *Prog. Cell Cycle Res.*, **5**: 309 – 325.

3. Woods, J.A., Hadfied, J.A., Pettit, G.R., Fox, B.W., McGown, A.T. (1995) The interaction with tubulin of a series of stilbenes based on combretastatin A-4. *B. J. Cancer*, **71**: 705 – 711.

4. Torricelli, A., Pifferi, A., Taroni, P., Giambattistelli, E. and Cubeddu, R. (2001*) In vivo* optical characterization of human tissues from 610 to 1010 nm by time-resolved reflectance spectroscopy. *Phys.Med.Biol.*, **46**: 2227–2237.

5. Botchway, S.W., Parker, A.W., Bisby, R.H. and Crisostomo, A.G. (2008) Real-time cellular uptake of serotonin using fluorescence lifetime imaging with two-photon excitation. *Microsc.Res.Tech.*, **71**: 267 – 273.

6. Greenspan, P., Mayer, E.P. and Fowler, S.D. (1985) Nile Red: A selective fluorescent stain for intracellular lipid droplets. J.Cell Biol. **100**: 965-973

7. Lin, C.M., Ho, H.H., Pettit, G.R. and Hamel, E. (1989) Antimitotic natural products combretastatin A-4 and combretastatin A-2: Studies on the mechanism of their inhibition of the binding of colchicine to tubulin. Biochemistry **28**: 6984-6991

The plant secretoryome: protein-protein interactions in the higher plant secretory pathway

Contact *c.hawes@brookes.ac.uk*

Chris Hawes, Imogen Sparkes, Anne Osterrieder, Jennifer Schoberer.
School of Life Sciences, Oxford Brookes University, Oxford, OX3 0BP

Stanley Botchway, and Andy Ward
Central Laser Facility, STFC, Rutherford Appleton Laboratory, Harwell Science & Innovation Campus, Didcot, OX11 0QX

Introduction

Work in the Plant Cell Biology Group at Oxford Brookes is centered around the structure and function of the organelles of the higher plant secretory pathway.

This report summarises a continuing series of experiments that were carried out to investigate the interactions between plant Golgi matrix proteins and regulatory GTPases, new projects on the interactions of plant Golgi transferase enzymes and the oligomerisation of storage proteins in the endoplasmic reticulum (ER), plus interaction between myosin tail domains and Rab GTPases. We also summarise progress on the development of a TIRF based laser tweezer instrument.

Plant Golgi Matrix Proteins:

Proteins do not reach their location within the secretory pathway instantly but require a certain amount of time in which they might be located in different compartments and therefore are exposed to different environments. In our case, it cannot be distinguished by eye whether our marker is located at ER exit sites or Golgi bodies, as the localisation signals look the same. However, as fluorescence lifetime is dependent on the fluorophore's surroundings, its lifetime might be different in the ER or Golgi lumen and affect our interpretation of putative protein binding. We therefore measured the lifetimes of our GFP control at day two, three and four after transfection. The control lifetimes appeared to be constant throughout, reassuring us that changes in lifetimes were most likely due to co-expression of binding partners and not due to external influences on the control.

We continued to screen for putative interactions of the *cis*-Golgi matrix protein AtCASP, focussing on the small GTPases SAR1A, SAR1B and ARF1 which are key players in orchestrating COPI and COPII-mediated protein trafficking. We observed no interaction between AtCASP and ARF1. Interestingly, in case of AtCASP and SAR1A or SAR1B, the GFP lifetime appeared to be significantly reduced in a small subset of Golgi bodies and only in a few cells. This might indicate that binding between these proteins is spatially or temporally very restricted, or happens transiently. Alternatively, the orientation of the attached fluorophores might not be too favourable for energy transfer to occur in an efficient manner, leading to a slight reduction lifetime. We also tested binding of the Golgi tethering factor GC2 to microtubules, but did not observe a reduction in lifetime. Measurements were difficult to carry out though, as the microtubule marker labels long filaments and the cytoplasm, whereas GC2 locates to the rims of Golgi bodies, resulting in a very narrow region of overlap between the two.

Plant Golgi transferase interactions:

Even after decades of research, the mechanisms responsible for the localisation of glycan processing enzymes, the major class of Golgi integral membrane proteins, within the plant Golgi apparatus have remained uncertain. One of the proposed retention mechanisms is based on the formation of homo- and/or hetero-oligomers of enzymes residing in the same or adjacent Golgi cisternae. In mammals there is compelling evidence in favour of an oligomerisation of *cis*-/medial-Golgi as well as medial-/*trans*-Golgi enzymes. However, evidence for similar events in plants is still lacking.

We have cloned a multitude of Golgi-located enzymes and analysed the subcellular localisation of the full-length enzymes as well as truncations thereof containing only their transmembrane domain and flanking regions, by confocal microscopy. Photobleaching experiments suggested an unhindered mobility of those enzymes in Golgi membranes and hence we concluded that they do not seem to be physically restrained by a potential complex formation, consequently arguing against potential oligomerisation retention mechanisms.

To ultimately confirm our hypothesis, we used the two-photon FRET-FLIM set-up to test for interactions *in planta* between four different *cis*-/medial-Golgi plant *N*-glycan processing enzymes, namely full-length versions of MNS1 (mannosidase 1), MN3 (mannosidase 3), GnTI (N-acetyl glucosaminyl transferase 1) and GMII (Golgi mannosidase 2). N-terminal GFP and RFP fusions were constructed for FRET and every possible combination of enzymes was tested. Surprisingly we found that each of the four enzymes interacted either with itself or at least with one of the other enzymes or both. In detail, the following results were obtained: A clear interaction was observed between GnTI with itself, MNS1 and MNS3, plus MNS1 with itself. Potential interactions of GMII with MNS3 and GnTI were observed which will be tested further.

This unexpected result provides the first experimental evidence in plants for the oligomerisation of *N*-glycan processing enzymes residing in close proximity to each other.

Endoplasmic reticulum protein interactions:

We continued our study of proteins that control the morphology of the endoplasmic reticulum. Using FRET-FLIM we tested whether RHD3, an ER membrane protein implicated in ER tubule organisation, interacts with reticulons, a family of ER shaping proteins. The expected results were that RHD3 would interact with reticulons, however the lifetime values do not reflect an interaction. However, this interaction has since been tested biochemically and shown to occur.

Myosin interaction with Rab GTPases:

We have started to look at potential interactions between Rab GTPases and myosin tail domains using N terminal fusions to mRFP and eGFP. Initial lifetime values recorded indicated that there may be a slight reduction in lifetime. This will be repeated.

Trafficking of wheat storage proteins in tobacco:

Prolamins, the main storage proteins of wheat seeds, are synthesized and retained in the endoplasmic reticulum (ER) of the endosperm cells, where they accumulate in protein bodies (PBs) and are then exported to the storage vacuole. The mechanisms leading to these events are unresolved. To investigate this unconventional trafficking pathway we fused

wheat γ-gliadin and its isolated repeated N-terminal and cysteine-rich C-terminal domains to fluorescent proteins and expressed them in tobacco leaf epidermal cells. Our results indicated that γ-gliadin and both isolated domains were able to be retained and accumulated as protein body-like structures (PBLS) in the ER, suggesting that tandem repeats are not the only sequence involved in γ-gliadin ER retention and PBLS formation. We also report on the high actin-dependent mobility

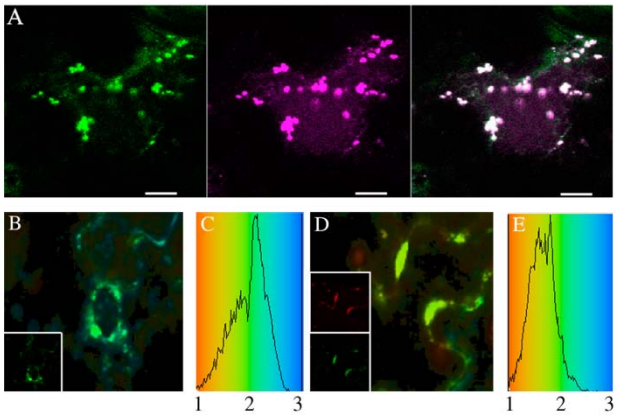

Figure 1. A. Expression of C terminal-γ-gliadin-GFP and N terminal-γ-gliadin-RFP in tobacco leaves showing co-localisation of the protein bodies. B-F. FRET-FLIM analysis in tobacco leaf epidermal cells. Lifetime images of Cter-γ-gliadin-GFP (B), and Cter-γ-gliadin-GFP in a cell coexpressing Nter-γ-gliadin-mRFP (D) are shown. Insets are confocal images showing expression of Nter-γ-gliadin-mRFP (red) and or Cter-γ-gliadin-GFP (green) in the cells shown. C,E Curves of B & E showing reduction in GFP lifetime in co-expressing cells.

of γ -gliadin PBLS, and demonstrate that most of them do not colocalize with Golgi body or prevacuolar compartment markers. Both γ -gliadin domains are found in the same PBLS when coexpressed, which is most likely due to their ability to interact with each other as indicated by the yeast two-hybrid experiments. To confirm this data *in vivo* we applied a FRET/FLIM strategy. Tobacco leaf epidermal cells expressing either C-terminal γ-gliadin fused to GFP or in combination with N-terminal γ-gliadin fused to mRFP were excised and interaction tested. The fluorescence lifetime of C-terminal γ-gliadin fused to GFP in cells coexpressing both N and C terminal γ-gliadin fusions was significantly reduced compared to cells only expressing C-terminal γ-gliadin GFP (1.70 +/- 0.12ns s.d. compared to 2.19 +/-0.1ns s.d. respectively $p < 0.001$ t-test). The significant reduction of more than 0.1ns indicated that in plants N and C terminal domains of γ-gliadin did in fact interact, confirming the yeast 2 hybrid studies (Francin-Allami *et al*. 2011).

Development of Laser Tweezers on a TIRF microscope

Last year we reported on the construction of TIRF-based laser tweezer microscope based around a Nikon TE-200-S inverted TIRF microscope with a 1.49NA oil immersion objective. Imaging is carried out with a 473nm diode laser and trapping with a 1064 Nd:YAG diode laser focused to the imaging plane of the microscope. Experiments were carried out on tobacco and arabidopsis leaves and successful trapping of Golgi bodies was achieved. The instrument is now prepared for routine use and will be used in an investigation of Golgi connections to the ER in leaf cells.

Acknowledgements

This work was supported by a BBSRC grant to C. Hawes (BB/F008147/1) and a Schrodinger Fellowship from the Austrian Government to J. Schoberer

References

1. Francin-Allami, M., Saumonneau, A., Lavenant, L., Bouder, A., Sparkes, I., Hawes, C. & Popineau, Y. (2011). Dynamic trafficking of wheat γ-gliadin and of its structural domains in tobacco cells, studied with fluorescent protein fusion proteins. Journal of Experimental Botany, *in press*.

Probing the Mechanism of Blue Light Sensing BLUF Domain Proteins: A Study Through Transient Infra-red Spectroscopy, Isotope Editing and Mutagenesis

Contact *s.meech@uea.ac.uk*

Andras Lukacs
University of East Anglia
Norwich NR4 7TJ

Rui-Kun Zhao
University of East Anglia
Norwich NR4 7TJ

Allison Haigney
Stony Brook University
New York 11794-3400, USA

Richard Brust
Stony Brook University
New York 11794-3400, USA

Gregory M. Greetham
Research Complex at Harwell
Central Laser Facility

Michael Towrie
Research Complex at Harwell
Central Laser Facility

Peter J. Tonge
Stony Brook University
New York 11794-3400, USA

Stephen R. Meech
University of East Anglia
Norwich NR4 7TJ

Introduction

Flavoproteins are a large family of proteins that contain a covalently or non-covalently bound flavin cofactor.[1] Although the isoalloxazine ring of the flavin functions predominantly as an electron transfer intermediate in biochemical oxidation-reduction reactions, there are at least three subfamilies of flavoproteins that function as photoreceptors: the light-oxygen-voltage (LOV) domain proteins, the cryptochromes, and the Blue Light Using FAD (BLUF)-domain proteins.[2] The chromophores in other well known photoreceptors such as the rhodopsins, xanthopsins and phytochromes undergo an isomerization when light is absorbed. However, this is not the case for flavoprotein receptors. Consequently there is substantial interest in understanding how absorption of light by the flavin is coupled to the conformational change(s) that lead to the signaling state. In the LOV domain proteins a cysteinyl-flavin adduct is transiently formed in the signaling state. However, in the cryptochromes and BLUF proteins, the initial structural changes resulting from photoexcitation are less well established.

The most extensively studied BLUF domain protein is AppA, an anti-repressor involved in controlling photosystem biosynthesis in the photosynthetic bacterium *Rhodobacter sphaeroides.* In the dark, AppA binds PpsR, a transcription factor, forming an AppA-$PpsR_2$ complex. When irradiated with blue light, the complex dissociates releasing PpsR, which can then bind to DNA and repress photosystem biosynthesis. Photoexcitation of AppA to form the signaling state is characterized by a 10 nm red shift in the 445 nm electronic transition of the isoalloxazine chromophore, and is known to involve strengthening of hydrogen bonds between the C4=O group of the chromophore and the protein. However, the mechanism leading to these structural changes and how they relate to BLUF domain activity remain to be fully elucidated. A plausible model for the BLUF photocycle has been proposed based on ultrafast transient absorption spectroscopy of AppA.[3] In this model, the light activated state of AppA (lAppA) is formed via an electron transfer that leads to formation of the anionic FAD semiquinone ($FAD^{\bullet -}$) followed by proton transfer leading to the formation of the neutral semiquinone ($FADH^{\bullet}$), and finally to lAppA in which the FAD has returned to its fully oxidized state. Subsequent photon absorption by lAppA is then proposed to lead to $FADH^{\bullet}$ which relaxes back to lAppA explaining the absence of rapid photoreversibility.

Since the FAD is fully oxidized in both the dark and light adapted forms of AppA (dAppA and lAppA, respectively), transient changes in the electronic structure of the FAD isoalloxazine ring must trigger a metastable change in the protein environment that surrounds the cofactor and that distinguishes dAppA and lAppA. While several proposed structural changes are involved in formation of the signaling state, all suggest an alteration of the Q63 hydrogen bonding interactions with FAD. Anderson and co-workers proposed a model where Q63 rotates upon light absorption resulting in cleavage of the hydrogen bond to the N5 of the flavin and formation of a new hydrogen bond to the flavin O4 carbonyl oxygen (Figure 1).[4] This rotation causes a rearrangement in hydrogen bonding which includes the formation of a new hydrogen bond from the hydroxyl side chain of Y21 to the amide side chain of Q63 and disruption of the hydrogen bond to the nearby W104. Such structural changes should have observable consequences for the (transient) infra-red spectrum. Based on additional structural data and quantum chemical calculations, a more recent model proposes that Q63 tautomerizes after light absorption, resulting in the rearrangement in the hydrogen bonding network around the flavin chromophore.

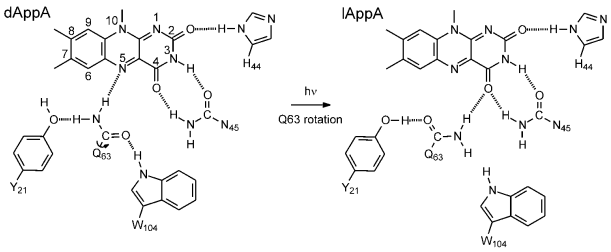

Figure 1. Changes in structure and H-bonding pattern associated with signaling state formation in AppA.

In the series of experiments described below we probe in detail the mechanism of operation of the BLUF domain of AppA. The methods we use are ultrasensitive ultrafast transient infra-red spectroscopy, using the ULTRA facility at the Research Complex at Harwell, and ultrafast transient optical spectroscopy (at UEA). To better elucidate the mechanism we use

isotopically edited proteins and isotope labeled flavins, which allows us to distinguish modes of the protein perturbed by optical excitation from modes arising from the flavin chromophore itself. To permit better characterization of the transient flavin modes we study the spectroscopy and dynamics of FAD in its oxidized, radical and fully reduced states. This allows us to identify any intermediate reduced states formed in the photocycle. Finally we use point mutagenesis to modify specific amino acid residues which may be implicated in the light sensing mechanism.

Experiments

The ULTRA facility has been described in detail elsewhere, and it can be used for a wide variety of ultrafast laser experiments. The measurements described below exploit the high repetition rate and stability of the ultrafast IR source to measure linear IR transient absorption following excitation of the flavin by a sub 100 fs 400 nm pulse (pump). The time resolved IR (TRIR) experiment measure intensity normalized transient IR difference spectra (pump pulse on minus pump pulse off). With this apparatus we are able to measure photoinduced changes in the IR transmission with accuracy of 1 μOD. Such high sensitivity is critical for experiments where the sample is photoactive, the concentration cannot be too high and the total amount of the sample is small; all of these restrictions apply to the BLUF domain proteins, their mutants and isotopologues.

The complementary ultrafast optical transient absorption measurements use a 1 kHz source with 400 nm pump and white light continuum probe. High sensitivity is obtained with CCD detection.

For all experiments on photoactive samples the IR sample cell is rastered in the beam and the sample is flowed using a low volume flow cell. The pump energy per pulse is kept below 200 nJ to avoid multi-photon effects.

Isotope studies of TRIR spectra

Our preliminary studies of FAD in buffer and bound to AppA revealed important similarities, which permitted assignment of the main vibrational modes, but also some significant differences, which suggested the appearance of protein modes in the TRIR spectrum of AppA.[5] This is an important result as it suggests coupling between the FAD excitation and the protein matrix on an ultrafast time scale. The result also presents the problem of how to resolve FAD modes from protein modes. To address this we initiated a series of TRIR studies of FAD isotopes, both in solution and bound to AppA; where FAD isotopes were not available riboflavin was bound to AppA. Initial experiments focused on [2-$^{13}C_1$]-FAD and [4,10a-$^{13}C_2$]riboflavin.[6]

The time-resolved IR data for FAD and riboflavin bound to AppA are similar in peak position, dynamics and intensity. This result confirms the assumptions made from steady-state experiments that riboflavin is a good model for FAD in the BLUF domain of AppA. On the basis of this information, we are confident that both riboflavin and FAD can be used interchangeably as models to study flavin excited state dynamics of AppA. Isotope labelling of FAD and riboflavin enabled the assignment of various ground and excited state modes observed in the TRIR spectra of AppA (Figure 2). Specifically, the high-frequency and low-frequency carbonyl modes are confidently assigned as mainly C4=O and C2=O localized modes, respectively. However, isotopic exchange and DFT calculations showed that these modes have significant mixed character notably N3H wag which is medium dependent. In addition, the 1660-1670 cm^{-1} transient absorption previously reported[5] as a photoactive marker has been designated a protein-chromophore band based on the changes seen upon isotope labelling. Perhaps most significantly the pair of high frequency carbonyl modes were shown to have character intermediate between isolated C=O stretch/N3H wag and symmetric – antisymmetric oscillations of the O=C4-N3H-C2=O group. The character of this pair of modes was shown to be sensitive to the local H-bonding environment, and thus a sensitive probe of the interaction between FAD and the protein matrix.[6]

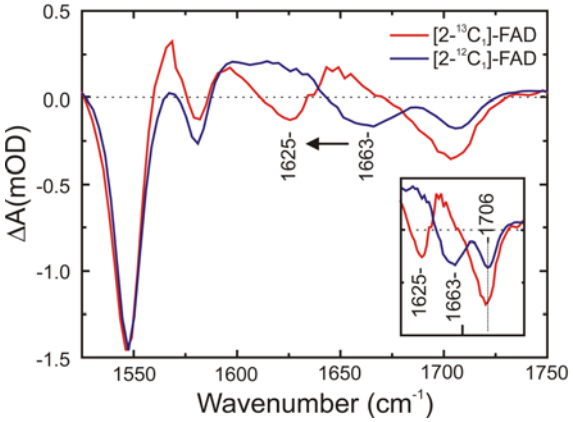

Figure 2 TRIR and calculated spectra of unlabeled FAD and [2-$^{13}C_1$]FAD in H_2O. FAD concentration was 6 mM in phosphate buffer, pH 8, and the TRIR spectra were recorded with a time delay of 3 ps

We have now extended these measurements to a series of ^{13}C, ^{18}O and ^{15}N isotopes, to achieve a rather complete assignment of the AppA spectrum. For example ^{13}C substitution on the xylene ring allows, when complemented by DFT calculations, assignment of the most intense bleaches seen in FAD TRIR. (Figure 3).[7]

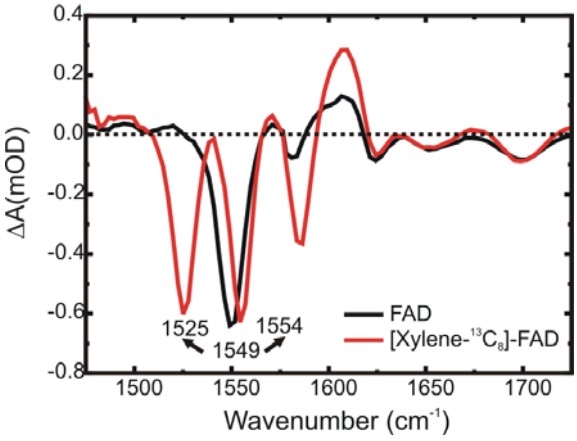

Figure 3 TRIR spectra of unlabeled FAD and [Xylene-$^{13}C_8$]-FAD in D_2O.TRIR spectra of 3 mM FAD (black) [Xylene-$^{13}C_8$]-FAD (red) in pD 8 phosphate buffer recorded with a time delay of 3 ps

Model studies of FAD oxidation states

Many of the proposed models for the BLUF photocycle suggest a role for excited state electron transfer quenching of the excited flavin, by surrounding protein residues (especially tryptophan and tyrosine). However, the complex kinetics observed (see below) and the broad unstructured nature of the electronic spectra of the radical states proposed as intermediates mean that the conclusions reached concerning the mechanism are rather speculative. In principle TRIR spectra will be more characteristic of a given intermediate state and thus permit better characterization of the photocycle. Our original experiments did not clearly identify any new states formed after excitation.[5] Consequently, we initiated a series of studies of FAD in different redox states ($FAD^{\bullet-}$, $FADH^{\bullet}$, $FADH^{-}$, $FADH_2$).

The transient IR and electronic spectra of two fully reduced forms of FAD ($FADH^-$, $FADH_2$) were measured.[8] Both have excited state decay times on the tens of picoseconds timescale. Measurements of the ground state recovery show that the mechanism of radiationless decay is internal conversion. There is a short lived bottleneck in the ground state recovery cycle, possibly a vibrationally hot form of the ground state. The protonated form $FADH_2$ has a faster excited state decay than $FADH^-$. The latter exhibits an unexpected inverse deuterium isotope effect (Figure 4). This is ascribed to the role of an H-bonded mode in determining the radiationless relaxation rate. This also provides a route whereby the flavin environment may influence the excited state decay kinetics, for example through H-bonding with the protein matrix. Vibrational modes in the ground state associated with the two carbonyl groups were observed and assigned on the basis of DFT calculations. Experimental data also revealed the corresponding frequencies in the excited electronic state. Such data can be used to assign transient photo induced electron and proton transfer reactions in proteins involving fully reduced forms of the flavins.

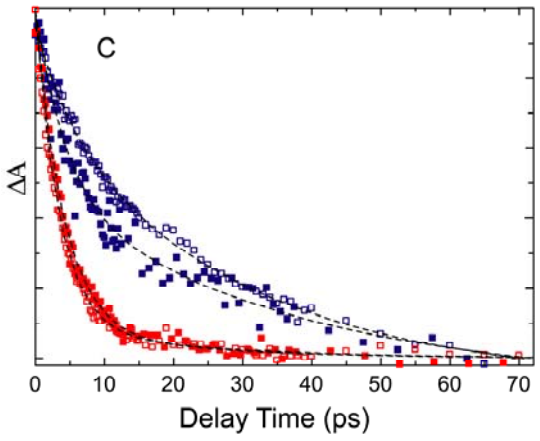

Figure 4 Deuterium isotope effect on the transient absorption of $FADH/D_2$ (red) and $FADH/D^-$ (blue) at 500 nm (Open symbols H, Filled D)

These experiments were extended to the radical states ($FAD^{\bullet-}$, $FADH^{\bullet}$), which are proposed intermediates in the BLUF photocycle.[9] These present extra difficulties due to their instability in solution. We first synthesised a radical state known to be moderately stable, and characterised its spectra and dynamics. We then prepared metastable radical states in the flavoproteins glucose oxidase and flavodoxin, and characterized separately their TRIR spectra and ultrafast dynamics.

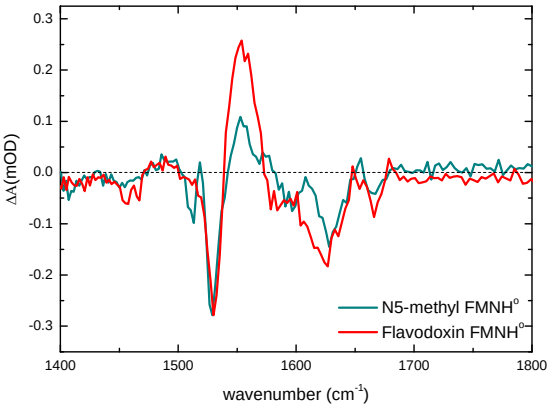

Figure 5 Comparison of TRIR spectra of N5-methyl $FMNH^o$ and $FMNH^o$ in flavodoxin.

The photophysical properties of N5-methyl $FADH^o$ and N5-methyl $FMNH^o$ radicals were studied by the means of transient visible and TRIR spectroscopy. These are the first transient IR studies of flavin radical states (Figure 5). We found that the excited state lifetime of these methylated flavin radicals is ~13 ps in aqueous solution. We also measured the transient infrared spectra of flavodoxin and glucose oxidase when their flavin cofactor was in the neutral radical state; we also measured the spectrum of glucose oxidase with its cofactor in the anionic radical state. These spectra will be critical for characterizing the BLUF photocycle. We found that the excited state decay of FMN was very much shorter in one protein (flavodoxin) than in solution, on the other hand the excited state of the neutral flavin radical in GOX decayed more slowly than in solution.[9]

Protein chromophore coupling

Equipped with these quite detailed TRIR assignments it is possible to attempt to discriminate between modes due solely to the excitation of FAD in AppA and modes which appear in the IR spectrum as a consequence of excitation induced changes in the protein. Clearly the latter are of primary interest in understanding the primary steps in the photocycle. A particularly interesting and clear cut example is to be found in the mutant Q63E. The Q63 residue is critical in the BLUF photocycle (Figure 1). The Q63E mutation places a symmetrical carboxylate (or carboxylic acid, depending on pK_a)) near the flavins, so the isomerization cannot lead to photoactivity by the mechanism in Figure 1. In line with this the mutant is photoinactive. However, the TRIR spectrum in rather interesting in that a new mode appears as a bleach at an unusually high frequency (1724 cm^{-1}).[10] No such mode if found in either dark or light adapted AppA (Figure 6). The remaining TRIR modes for Q63E are intermediate between AppA in its light and dark adapted states, consistent with it being photoinactive.

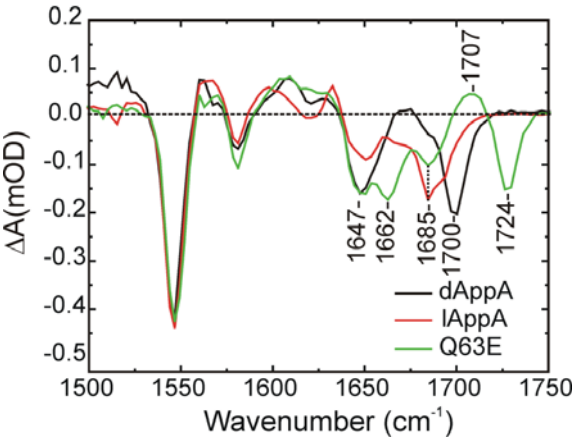

Figure 6 TRIR spectra of $dAppA_{BLUF}$ (black), $lAppA_{BLUF}$ (red) and Q63E $AppA_{BLUF}$ (green) bound to FAD. Protein concentration was 2 mM in pD 8 phosphate buffer and the TRIR spectra were recorded with a time delay of 3 ps. The spectra have been normalized to the intense FAD ring bleach mode at 1547 cm^{-1}.

It was further observed that this mode appears within the 100 fs time resolution of the experiment. Such a prompt appearance suggests is may be associated with an FAD ground state mode shifted up in frequency in Q63E. However, in model studies we found no such large up-shift in a carbonyl frequency under any conditions. Further using the C4=^{18}O FAD isotope did not shift the frequency at all. This suggests that the 1724 cm^{-1} mode may be assigned to protein. To confirm this fully ^{13}C labeled AppA was prepared [U^{13}C Q63E AppA] was prepared. This lead to a downshift in frequency of the 1724 cm^{-1} mode, confirming it to be of protein origin (Figure 7). This result leads to two significant conclusions. First, the electronic spectrum of FAD is hardly perturbed by the Q63E mutation, in fact the Q63E spectrum is intermediate between lAppA and dAppA, as expected. However, excitation of FAD leads to a frequency

shift of this mode within 100 fs. This is too fast for electron transfer, but suggests that the H-bond structure in the flavin binding pocket responds instantaneously to electronic excitation. Specifically we can conclude that excitation leads to a strengthening of the flavin E63 H-bond by ca 3 kcal/mol. Such changes in the H-bonding network may contribute to the initial stages of the photocycle, independent of any electron transfer steps. Second, the high frequency of the mode is consistent with an assignment to a carboxylic acid rather than a carboxylate. This is unexpected given that the pK_a of the glutamate suggests protonation at pH 8. This suggests that the binding pocket strongly favours neutral residues.

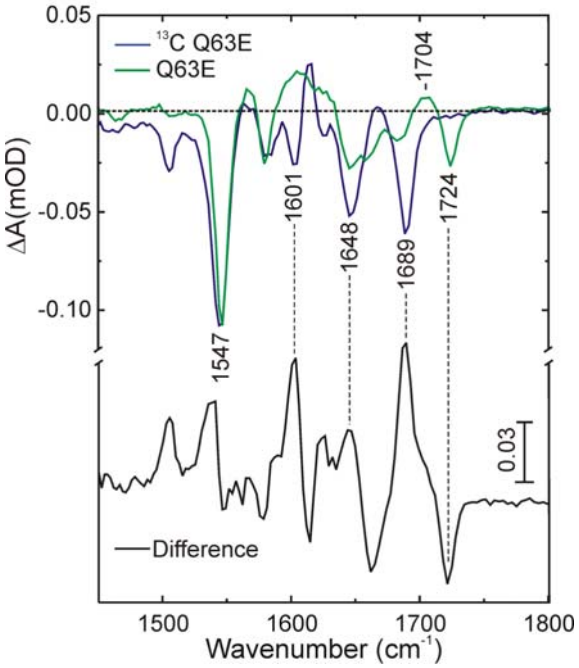

Figure 7. TRIR spectra of unlabeled and ^{13}C labeled Q63E AppA$_{BLUF}$ measured at 3 ps.TRIR spectra of unlabeled Q63E AppA$_{BLUF}$ (red) and ^{13}C labeled Q63E AppA$_{BLUF}$ (blue) bound to FAD. The difference spectrum is shown on the bottom panel (black). Protein concentration was 2 mM in pD 8 phosphate buffer and the TRIR spectra were recorded with a time delay of 3 ps. The spectra have been normalized to the intense FAD ring bleach mode at 1547 cm^{-1}.

Future Work

The mechanism of BLUF photocycle will be pinned down using a range of mutants, which have already been generated. The key Trp (W104) and Tyr (Y21) residues implicated in the electron transfer reactions have been exchanged for residues which cannot undergo electron transfer. Equipped with the reference spectra for the proposed intermediates we will be able to definitively establish the role of electron transfer in the BLUF domain. In a novel development we have made mutants with non-natural amino acids (fluoro tyrosines) which modulate the pKa and redox potential of the Y21 residue. This will provide a fine test of the role of this residue in electron and proton transfer reactions. We have also found that mutants of the S41 residue have a profound effect on the photocycle; these will be studies in detail.

We will extend our TRIR and transient absorption experiments to BLUF domains other than AppA. Specifically we have prepared the well know PixD BLUF domain, and the recently discovered, spectroscopically uncharacterized, BLUF domain responsible for phototaxis in bacteria.

An important objective is to extend the time over which the dynamics are observed from a few nanoseconds to several microseconds. In that way the structural changes of the protein following the initial photoinduced changes will be followed.

Conclusions

Important progress has been made towards understanding the mechanism of blue light sensing in BLUF domain flavoproteins. Careful assignments of the flavin modes have been made, allowing the discrimination of flavin from protein modes, and the identification of suggested reduced flavin intermediates. Similarly many of the possible intermediates in the proposed electron transfer reactions have been fully characterized. This has allowed the proper separation of protein modes from flavin modes. A particularly interesting result was obtained for the Q63E mutant, in which a protein made was bleached in <100 fs, indicating a coupling of the flavin excitation to protein structure which exists independent of any electron transfer reaction. Further mutants have been prepared to assess separately the roles of proton and electron transfer reactions in the BLUF photocycle.

Acknowledgements

We are grateful to STFC for the award of program access to the ULTRA facility, and the staff of that facility for their assistance. SRM and PJT were supported by an NSF-EPSRC joint research grant (EPSRC EP/G002916 and NSF CHE-0822587). Isotopes were kindly provided by the group of Prof. Adelbert Bacher.

References

1. A. Mattevi, *Trends in Biochemical Sciences*, 2006, **31**, 276-283
2. A. Losi, *Photochemistry and Photobiology*, 2007, **83**, 1283-1300
3. J. T. M. Kennis and M. L. Groot, *Current Opinion in Structural Biology*, 2007, **17**, 623-630
4. S. Anderson; Dragnea, V.; Masuda, S.; Ybe, J.; Moffat, K.; Bauer, C., Structure of a novel photoreceptor, the BLUF domain of AppA from Rhodobacter sphaeroides. *Biochemistry* **2005,** 44, (22), 7998-8005
5. A. L. Stelling, K. L. Ronayne, J. Nappa, P. J. Tonge and S. R. Meech, *Journal of the American Chemical Society*, 2007, **129**, 15556-15564
6. A. Haigney, A. Lukacs, R. K. Zhao, A. L. Stelling, R. Brust, R. R. Kim, M. Kondo, I. Clark, M. Towrie, G. M. Greetham, B. Illarionov, A. Bacher, W. Romisch-Margl, M. Fischer, S. R. Meech and P. J. Tonge, *Biochemistry*, 2011, **50**, 1321-1328
7. A. Haigney, A. Lukacs, R. K. Zhao, A. L. Stelling, R. Brust, R. R. Kim, M. Kondo, I. Clark, M. Towrie, G. M. Greetham, B. Illarionov, A. Bacher, W. Romisch-Margl, M. Fischer, S. R. Meech and P. J. Tonge In Preparation
8. R-K. Zhao, A. Lukacs, A. Haigney, R. Brust, G. M. Greetham, M. Towrie, P. J. Tonge and S. R. Meech Submitted for publication
9. A. Lukacs, R-.K. Zhao, A. Haighney, R. Brust, G. M. Greetham, M. Towrie, P. J. Tonge and S. R. Meech Submitted for publication
10. A. Lukacs, A. Haighney, R. Brust, R-.K. Zhao, I. Clarke, M. Towrie, G. M. Greetham, P. J. Tonge and S. R. Meech Submitted for publication

Kinetically stable metal complexes for multimodality PET/SPECT and optical fluorescence microscopy probed *in vitro* by FLIM

Contact *sofia.pascu@bath.ac.uk*

J.R.Dilworth, S. Faulkner M. W.Jones and P.A. Waghorn

University of Oxford
Inorganic Chemistry Department, South Parks Road, Oxford

S. I. Pascu and R.Arrowsmith

University of Bath
Chemistry Department, Claverton Down, Bath, Avon, BA27AY

S. W. Botchway and A. Parker

CLF
RAL, Harwell, Oxon

Introduction

Molecular imaging is a rapidly expanding field of global importance for both the diagnosis and personalised therapy of a range of disease states. The ability to detect and visualise abnormal or infected tissue in the body is critical for early and precise diagnosis of various forms of cancer, as well as neurological and cardiovascular diseases. A variety of technologies have been developed that allow a three-dimensional image of parts of the body to be generated with the aid of probe molecules that are accumulated at the site of interest (e.g. PET, SPECT, MRI, optical imaging). To determine the exact localisation and size of target tissue and visualise any disease-associated pathological changes, multi-modal techniques are frequently required, using the strengths of 2 or more techniques together. For instance, fluorescence-based optical imaging agents can often provide a very high degree of spatial resolution (below 1 micron), while the sensitivity of PET for the chemical concentration is the major strength of this technique. PET radiotracers can be detected down to the 100 picomolar level in target tissues., and at this low level the compounds often have little or no physiological effect on the patient (i.e. effectively non-invasive). In the context of cancer, there is an increasing demand for molecular probes that can be used for imaging and early detection of specific cancers which represent major life risks worldwide, such as breast, colon, and prostate cancer. The use of fluorescent probe molecules for the optical imaging of a range of cancer targets, such as prostate and breast cancers has been widely demonstrated, with selective imaging being achieved by tagging of a suitable probe with a

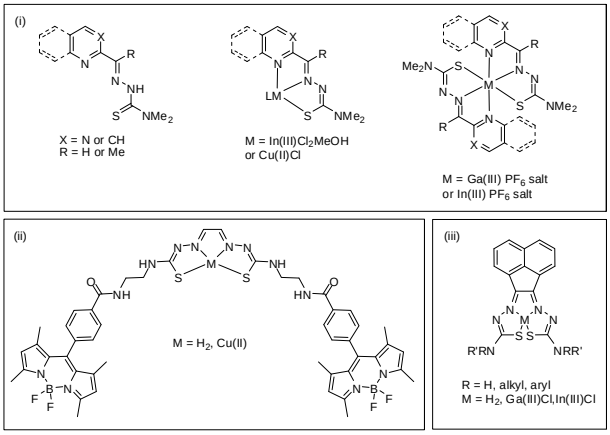

Figure 1 *Structures of the small molecule compounds studied in this session (i) tridentate pyrimidyl/quinolyl thiosemicarbazones, (ii) Bodipy conjugates of bis(thiosemicarbazones) (iii) acenaphthene thiosemicarbazone derivatives* [7]

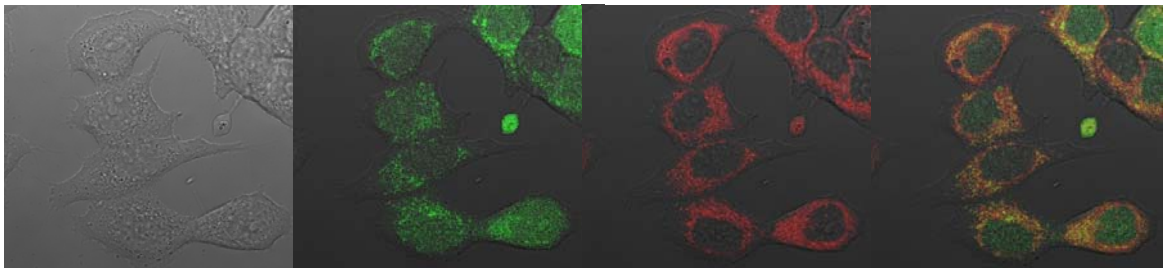

Figure 2 *Colocalisation confocal images of a new Indium thiosemicarbazide complex: (left to right) brightfield image of MCF-7 cells (2) the Indium complex (3) ER tracker (4) overlay of complex and ER tracker.*

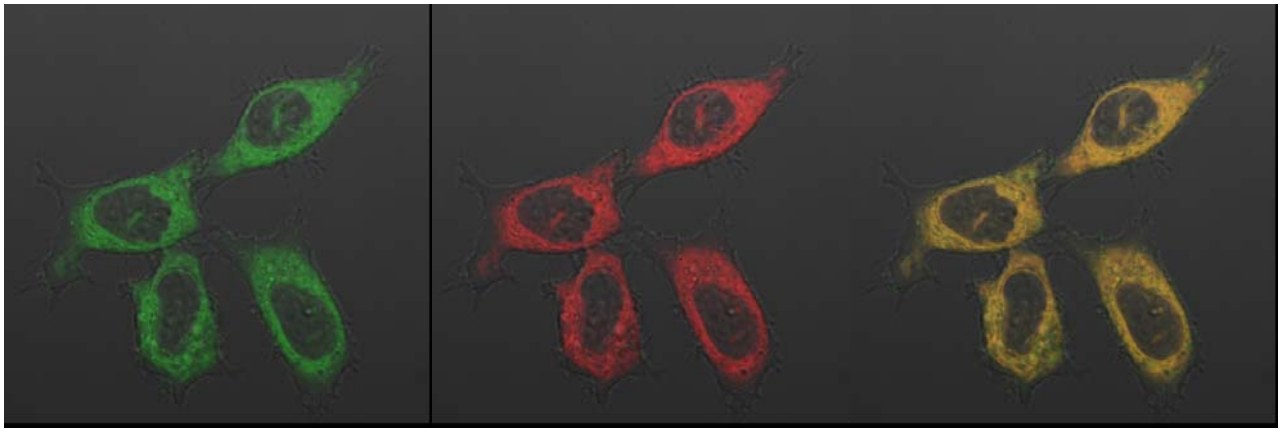

Figure 3 *Colocalisation confocal images of a ligand containing-Bodipy in HeLa cells: (left to right) (1) the ligand (3) ER tracker (4) overlay of compound and ER tracker.*

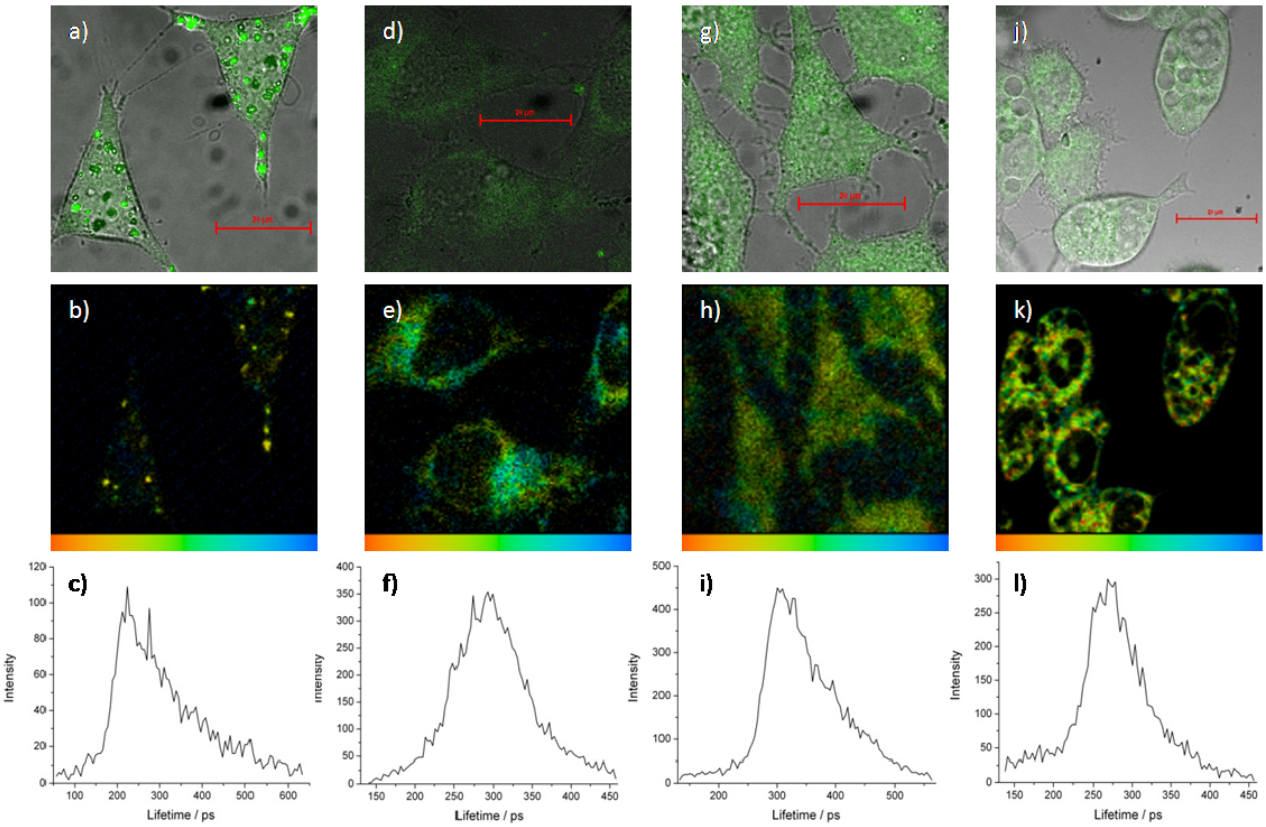

Figure 4: *a) 2-Photon Fluorescence emission map (λ_{ex} 910 nm), b) 2-Photon Fluorescence lifetime imaging map (λ_{ex} 910 nm) and c) corresponding lifetime distribution plots for the uptake of* ***4*** *at 50μM in HeLa cells after 1h incubation; d) 2-Photon Fluorescence emission map (λ_{ex} 910 nm), e) 2-Photon Fluorescence lifetime imaging map (λ_{ex} 910 nm) and f) corresponding lifetime distribution plots for the uptake of* ***D*** *at 50μM in HeLa cells after 1h incubation; g) 2-Photon Fluorescence emission map (λ_{ex} 910 nm), h) 2-Photon Fluorescence lifetime imaging map (λ_{ex} 910 nm) and i) corresponding lifetime distribution plots for the uptake of* ***6*** *at 50μM in HeLa cells after 1h incubation; j) 2-Photon Fluorescence emission map (λ_{ex} 910 nm), k) 2-Photon Fluorescence lifetime imaging map (λ_{ex} 910 nm) and l) corresponding lifetime distribution plots for the uptake of* ***6*** *at 50μM in PC-3 cells after 1h incubation.[7]*

targeting or address molecule. There is now intense interest in the application of similar targeted reagents for diagnosis, and monitoring treatment of cancer by PET, in particular the possibility of identifying and exploiting markers of cancer-relevant processes such as tumour hypoxia and angiogenesis. Shortage of oxygen (hypoxia) is a common cause of cancer treatment failure, so reliable imaging tools for tumour hypoxia would be invaluable in planning treatment regimens and predicting clinical outcomes. Confocal fluorescence microscopy has been used extensively to track compounds and follow processes in cells and we have designed a series of fluorescent metal complexes, that can be used for whole body imaging using gamma or positron emission and may be monitored in cells by virtue of their 1 or 2-photon excited fluorescence. We, and others, are particularly interested in complexes of metallic radionuclides and a key step in their biological action can be dissociation of the complex within cells. [1-6]

The emission lifetime and wavelength of a ligand changes when a metal is coordinated and this provides a potential method to determine when and where dissociation of a metal complex occurs within a cell. We have explored the use of this approach to determine if and when intracellular demetallation of biologically active metal complexes occurs.

New bis(thiosemicarbazone) complexes

The imaging materials explored here may be categorized into three distinct groups (i) tridentate pyrimidyl/quinolyl thiosemicarbazones, (ii) Bodipy conjugates of bis(thiosemicarbazones) (iii) acenaphthene thiosemicarbazone derivatives (Figure 1).

Results and Discussions

(i) Tridentate pyrimidyl/quinolyl thiosemicarbazones

The tridentate systems have been investigated as they bear a close semblance to Triapine (in Phase 2 clinical trials for advanced head and neck cancers) and numerous reports of metal complexes displaying potent biological activity i.e. anticancer, antiviral and antifungal. Limited nuclear uptake and perinuclear (nominally the endoplasmic reticulum (ER) or golgi bodies (GB)) localisation of some tridentates This was supported by colocalisation studies with nuclear (Hoechst) and ER (ER tracker) stains and also with fluorescence lifetime imaging microscopy (FLIM, Figure 2).

There was no evidence of uptake of the pyrimidine derivatives or their complexes due to negligible or weak fluorescence. This is currently being remedied by the attachment of a Bodipy fluorophore which will allow visualisation of the compounds *in vitro*.

The most crucial, result for this section of work was the intracellular speciation for the indium tridentate species i.e. bis- and mono- by FLIM, based upon the relative lifetimes of each of the species. This is a huge step forward and allows us to observe the decomposition pathway for the complexes and the intracellular site of this.

(ii) Bodipy conjugates of bis(thiosemicarbazones)

Following the report by Donnelly *et al.* [8] of the *in vivo* instability of GTS *cf.* ATS, a GTS analogue (an aldehyde derivative as opposed to a ketone derivative) with Bodipy fluorophores was prepared and investigated. Colocalisation confocal images indicated no nuclear, lysosomal or

mitochondrial uptake, but instead indicated perinuclear localisation in the ER and GB. This was consistent with earlier findings of related derivatives prepared by Waghorn (DPhil Thesis, Oxford 2010).

Images were obtained of several metal complexes of acenaphthene thiosemicarbazone derivatives (Figure 1, R = Me and allyl). In particular, it was noted that the cells' morphology was affected by the time point of the measurement, and were subsequently recorded at 20 min incubation (37^{o}C) instead of 1 h incubation time and using 0.5% DMSO. We argue that our compounds remain intact inside the cells within the 1 h observation time (Figure 4).

Summary

New confocal fluorescence imaging experiments were conducted on the test compounds outlined above. Our results show that it is possible to discriminate between free ligand and that of the complex in cells and, although the quantification of the degree of dissociation has not been demonstrated, these approach demonstrated that in vitro FLIM methods are crucial in understanding the behaviour of metal complexes in cells and may become a key technique in the development of new imaging metallodrugs.

Conclusions

Sub-nanosecondexcited state lifetime resolved following 2-photon microscopy has clear potential as a tool for investigating the speciation of metal complexes in cells and *in viscera*. Much remains to be done, and we are currently focusing on probing the speciation of these complexes further, and on the development of new methods for image analysis and processing.

Several key findings were made, including intracellular localisation, speciation based on FLIM and proof of principle for GTS derivatives. This work has aided the biological investigation of these compounds and is under preparation for a publication.

Acknowledgements

Royal Society and the University of Bath are acknowledged for funding the Bath teams' participation in all experiments.

References

1. M. P. S. Dunphy and J. S. Lewis, *Journal of Nuclear Medicine*, 2009, 50, 106-121

2. Finch, Rick A.; Liu, Mao-Cin; Grill, Susan P; Rose, William C.;Loomis, Regina; Vasquez, Kren M.; Cheng, Lui-Chi; Sartorelli, Alan C. *Biochemical Pharmacology*, (2000), 59, 983-991

3. Wei, Lihui; Easmon, Johnny; Nagi, Ravneet K.; Meugge, Brian D.; Meyer, Laura A. and Lewis, Jason S. *Journal of Nuclear Medicine*, (2006), 47, 2034-2041

4.Bailey, Kristy E.; Costantini, Danny L.; Cai, Zhongli; Scollard, Deborah A.; Chen, Zhuo; Reilly, Raymond M.; Vallis, Katherine A. *Journal of Nuclear Medicine* (2007), 48(9), 1562-1570

5. Pascu, S. I.; Waghorn, P. A.; Kennedy, B. W.C.; Arrowsmith R. L.; Bayly, S. R.; Dilworth, J. R.; Christlieb, M.; Tyrrell, R. M. ; Zhong, J.; Kowalczyk, R. M.; Collison, D. ; Aley, P. K. ; Churchill, G. C. and Aigbirhio, F. I. *Chem.- Asian. J*., **2010**, 5, 506 – 519 (invited article for special issue: In recognition of 150 years of UK Japan diplomatic relations).

6. Pascu, S. I.; Waghorn, P. A.; Conry, T.; Lin, B.; James C. and Zayed, J.: *Advances in Inorganic Chemistry***, 2009**, 61, 131-178. DOI: 10.1016/S0898-8838(09)00203-7

7. Rory L. Arrowsmith, Philip A. Waghorn, Michael W. Jones, Andreas Bauman, Simon K. Brayshaw, Zhiyuan Hu, Gabriele Kociok-Köhn, Thomas L. Mindt, Rex M. Tyrrell, Stanley W. Botchway, Jonathan R. Dilworth and Sofia I. Pascu *Fluorescent gallium and indium bis(thiosemicarbazonates) and their radiolabelled analogues: Synthesis, structures and cellular confocal fluorescence imaging investigations* ***Dalton Trans.***, 2011, Advance Article **DOI:** 10.1039/C1DT10126A

8. Donnelly *et al.*, JBC, 2008, 283, 4568)

Porous Carbon Microspheres: Solution Phenomena and Cellular Uptake

Contact *susan.quinn@ucd.ie*

S. J. Quinn, L. M. Magno

School of Chemistry and Chemical Biology, University College Dublin, Dublin 4, Ireland

P. E. Colavita, P. Duffy

School of Chemistry, Trinity College Dublin, Dublin 2, Ireland

R. Yadav, S. K. Roberts, A. D. Ward, S. W. Botchway

Central Laser Facility, Rutherford Appleton Laboratory, Harwell Science & Innovation Campus, Didcot, OX11 0QX

Introduction

Carbon based materials are attractive for biological applications as they are chemically inert, can be easily functionalized and have an excellent biocompatibility profile. The chemical versatility of carbon has led to substantial research of carbon materials in the areas of biotechnology and biomedicine.[1] At the nanoscale single-walled carbon nanotubes (SWNTs) have been found to cross the cell membrane and their optical properties have been exploited for intracellular sensing.[2,3] These studies have recently been extended to carbon quantum dots.[4] However, the exploitation of microscale carbon particles for cellular applications remains unexplored. Mesoporous materials hold great promise as delivery agents.[5] Porous carbon microspheres are attractive for a number of reasons. They can be prepared via a routine synthesis. They are easy to handle and purify, and are readily functionalized. Porous carbons with high specific surface area are particularly interesting because it is possible in principle to leverage their properties to deliver high drug payloads. We are interested in these materials for the purposes of cell imaging and delivery. In this report we present findings of our study of the fundamental solution properties of porous carbon microspheres (pCμS) in solution using Raman optical tweezers. We further report the use of fluorescence confocal microscopy imaging to show the uptake of fluorescently labelled microspheres by cells and our ability to leverage their optical absorptivity in order to cause carbon graphitization and cell death.

Experimental

Combined Raman-optical tweezer studies were carried out using a previously described setup.[6,7] For trapping and acquisition of Raman spectra the laser was attenuated to a power of 16 mW, measured at the entrance aperture of the objective lens, yielding approximately 5 mW at the objective output. Raman spectra and trapping of carbon microspheres were recorded using capillary tubes to minimize thermal effects. Raman spectra of carbon particles were baseline subtracted using a spectrum of the background medium collected during the same measurement run. Spectra thus obtained were fitted to a Breit-Wigner-Fano line for the G peak, a Gaussian curve for the D peak[8] and a polynomial to remove any residual background using data analysis software (Igor Pro). High-resolution confocal images were obtained using a Nikon confocal laser scanning microscope, EC1-Si (CLSM) attached to an inverted Nikon TE2000-U microscope and a 60x water immersion objective (NA 1.2). For imaging carbon microspheres in cells particles functionalised with 6-aminofluorescein (FL-LiDCA) were used in combination with DiI as a cellular membrane probe. An argon ion and a helium-neon laser operating at 488 and 543 nm, respectively, were used alternately with line switching using the multi-track facility of the CLSM. Images were collected using a 488/543 dichroic beam splitter and a 512-530 band pass filter (channel 1) to detect fluorescence from FL-LiDCA particles, using a 560-615 band pass filter to detect fluorescence from the DiI membrane probe (channel 2) and using optical white light transmission (channel 3).

Results and Discussion

Raman optical tweezer study of carbon microspheres

Spherical pCμS were synthesized via ultraspray pyrolysis from aqueous precursor solutions of dichloroacetates at 700 °C, following methods developed by Skrabalak et al.[9] Use of a lithium precursor salt yielded particles with a surface area of ~ 1000 m^2/g (LiDCA). While use of a sodium precursor yielded particles area of 500 m^2/g (NaDCA), see Figure 1.

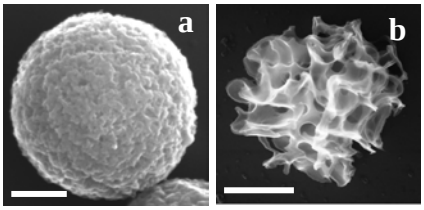

Figure 1. Scanning Electron Microscopy (SEM) images of (a; scalebar = 200 nm) LiDCA and (b; scalebar = 800 nm) NaDCA carbon microspheres synthesized via ultraspray pyrolysis using aqueous solutions of Lithium and Sodium dichloroacetate as organic precursors.

Individual particles could be either trapped in solution or pinned against the glass walls of the sample holder. Once in the optical trap, particles could be observed over prolonged times while simultaneously collecting Raman spectra, thus allowing the investigation of the behaviour of isolated particles. The Raman spectrum displays two peaks with maxima at 1597 rel. cm^{-1} and 1341 rel. cm^{-1} that are assigned to the G and D peaks respectively of amorphous carbon.[10, 11] The I(D)/I(G) ratios found for our particles suggest an sp^2 content >90% with a high degree of disorder. Raman-trapping experiments (λ_{exc}=532 nm) of single particles were conducted in a wide range of solvents and we observed significantly different behaviour. Single carbon particles suspended in water and ethylene glycol could be trapped and held for several minutes without observing any changes in their spectral signature; however, when particles were suspended in octanol and N,N-dimethylformamide (DMF) we observed intense and broad visible emission almost immediately after trapping. No significant difference was observed in this behaviour between LiDCA and NaDCA spheres. An example of a single particle emission event is shown in Figure 2a.

Figure 2b shows the difference Raman spectrum obtained by subtracting the octanol scattering contribution from spetra recorded over 16 s. The difference spectra show that, while the particle resides in the optical trap, its Raman spectrum evolves significantly. Th I(D)/I(G) ratio increases visibly from 0.56 to 2.2 and both the G and D peak maxima shift to lower values by up to ~20 cm^{-1} before returning close to their original positions. This behaviour is in contrast to results obtained in water, where

the carbon Raman spectrum remains unchanged over long times under the same conditions. These observations are consistent with graphitization and increase ordering arising due to thermal annealing. No emission was observed in water and ethylene glycol whereas immediate intense emission was seen in DMF and octanol. The solvent dependence of this phenomenon can be explained by considering the thermal conductivities of water, ethylene glycol, DMF and octanol which are 0.6071, 0.256, 0.184 and 0.161 W K^{-1} m^{-1} (at 298 K) respectively.[12] At constant incident laser irradiance it is easier to observe emission for suspensions prepared with solvents that display poor heat conduction, indicating that emissive behaviour, under our experimental conditions, is dominated by the heat conductivity properties of the surrounding medium.

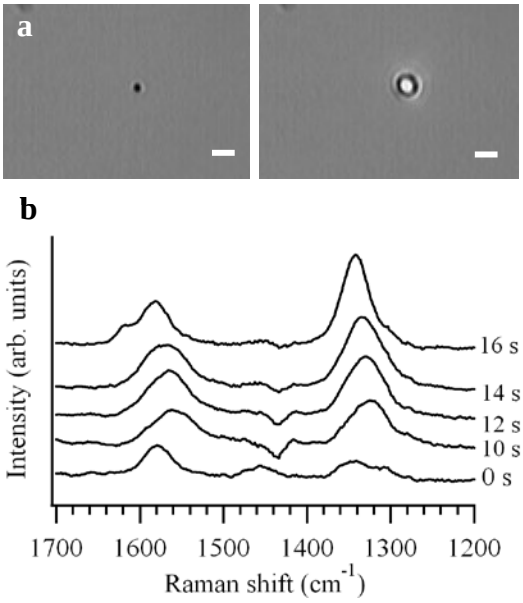

Figure 2. (a) Image of a single LiDCA particle before and after being optically trapped in octanol (scalebar = 3 μm). (b) Raman spectral changes displayed by a single carbon sphere in octanol monitored over 16 s; the octanol background has been and spectra have been smoothed and offset for the sake of clarity.

This hypothesis was investigated by changing the heat conductivity properties of the particle surroundings. Aqueous solutions of carbon microspheres in the presence of (a) the anionic surfactant sodium dodecyl sulfate (SDS) at 1% and (b) the cationic lipid, N-[1-(2,3-Dioleoyloxy)propyl]-N,N,N-trimethylammonium methylsulfate (DOTAP) at 0.04%, and Raman-tweezer studies performed. While it was possible to trap carbon spheres in both surfactant solutions, single particle emission was only found for the DOTAP system. Similarly, particle annealing was observed only in DOTAP aqueous solutions. The adsorption of ionic surfactants on solid surfaces is a complex process that results from a balance of electrostatic and hydrophobic interactions. It is known that surfaces that possess both hydrophobic and anionic sites (e.g. cellulose, activated carbons), as in the case of our particles, display higher adsorption rates and sorption capacity for cationic surfactants than for anionic surfactants.[13-16] DOTAP is therefore expected to adsorb more readily on carbon microspheres than SDS, creating an organic-like environment and thus reducing the heat conductivity in the immediate vicinity of the particles to a greater extent.

Intracellular studies

Human embryonic kidney (HEK293) and human epithelial carcinoma (HeLa) cells were incubated in the presence of fluorescently labelled LiDCA particles (FL-LiDCA) for 12 h at 37 °C using the cationic transfection agent FuGENE®. Confocal microscopy recorded fluorescein emission from dye labelled microspheres (λ_{exc}=488 nm) in both HEK293 and HeLa cells stained with the membrane dye DiI (λ_{exc}=543 nm). A complete depth profile (2 μm) of the cell was acquired by recording 30 scans at 150 nm intervals. Figure 3(a) and (b) shows images recorded 900 nm apart where the presence of the particles in the highlighted area is seen to change significantly. The z-travel distance over which disappearance/appearance of the microspheres were observed correlated well with the ~700 nm average size of the particles. The Z-scan in Figure 3c indicates that particles are distributed within the cytoplasm and are thus internalised by the cells. Figure 3d shows the transmission image overlayed with the fluorescence image for the fluorescein channel. Strong fluorescence was typically observed over the capture size of 78 μm^2; this suggests that particles are preferentially clustered in specific subcellular structures. These results indicate that carbon particles are uptaken by both cell lines and that molecules covalently linked to the surface of the microspheres, in our case a fluorescent dye, can be successfully delivered to the cytoplasm. The most likely mechanism for particle uptake is endocytosis which has been observed for similarly sized particles.[17] In our studies particle uptake was not seen to compromise cell viability and both cell lines remained viable for several days with normal cell division.

Optical trapping experiments were repeated on cells incubated in the presence of NaDCA and LiDCA particles. It was possible to trap and manipulate particles located both at the cell surface and within the cytoplasm, while at the same time obtaining their carbon Raman spectra. Once in the optical trap particles were found to display incandescence in a similar fashion to that observed in the presence of DOTAP. Furthermore, in cases where the particle was located near to the cell membrane the induced incandescence resulted in blebbing and membrane rupture. In other cases the incandescence resulted in complete membrane rupture with loss of intracellular material and cell death. Membrane rupture was also accompanied by changes in the carbon Raman signature, similar to those observed in media of poor heat conductivity indicating that carbon annealing and graphitization takes place also within cells. Importantly, no cell damage was observed due to the incident laser alone under the same conditions.

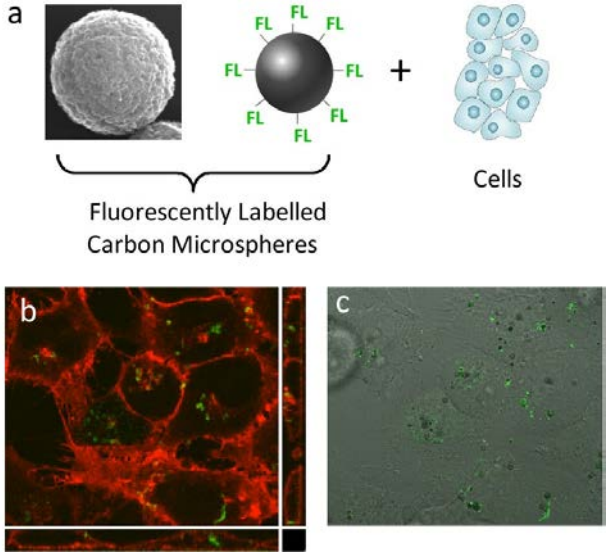

Figure 3. (a) Scheme showing addition of FL-LiDCA to cells. (b) Confocal image of HeLa cells after incubation with FL-LiDCA showing Z-scan rendering of carbon particle internalization in HeLa cells; the cell membrane is stained with DiI. and (c) Transmission image showing fluorescent nanoparticles.

Conclusions

In this work we have used Raman and optical trapping to demonstrate that absorption of 532 nm laser light by individual carbon mesoporous microspheres induces graphitization and incandescent emission. We have shown that this behaviour is

related to the ability of the environment that surrounds the microparticle to dissipate heat. We have also demonstrated that particles are successfully uptaken by cells using a commercial transfection agent. Particles bearing small molecules covalently linked to their surface can be carried by the carbon scaffold into the cytoplasm, thus opening the possibility of using these particles for delivery applications. Furthermore we have shown that when introduced in the cellular environment light absorption by particles can trigger membrane disruption and cell death. In summary, these results demonstrate that it is possible to leverage two important characteristics of mesoporous carbon materials: their ability to deliver small molecules to the cytoplasm and their high optical absorptivity. The high specific surface area of these mesoporous carbon microspheres suggests that they are an excellent platform for the development of delivery agents.

Acknowledgements

This work was carried out at the Central Laser Facility, STFC Rutherford Appleton Laboratory.[18] We are grateful to EPA Ireland for financial support through grant 2008-PhD-WRM-2 and to SFI (10/RFP/CAP2915) for funding of Dr. Luis Magno.

References

1. Bekyarova, E.; Ni, Y.; Malarkey, E. B.; Montana, V.; Williams, J. L.; Haddon, R. C. Parpura, V, *J. Biomed. Nanotech.* 2005, 1:3
2. Pantarotto, D.; Briand, J. P.; Prato, M.; Bianco, A. *Chem. Commun.* 2004, 16.
3. Kim, J.-H.; Ahn, J.-H.; Barone, P. W.; Jin, H.; Zhang, J.; Heller, D. A.; Strano, M. S.
4. Liu H, Ye T, Mao C *Angew. Chem.* 2007, 46, 6473.
5. Liong, M.; Angelos, S.; Choi, E.; Patel, K.; Stoddart, J. F.; Zink, J. I.; J. Mater. Chem., **2009**, 19, 6251.
6. Harvey, T. J.; Faria, E. C.; Henderson, A.; Gazi, E.; Ward, A. D.; Clarke, N. W.; Brown, M. D.; Snook, R. D.; Gardner, P. *J. Biomed. Opt.* **2008**, *13*, 064004.
7. Sanderson, J. M.; Ward, A. D. *Chem. Commun.* **2004**, 1120-1121.
8. Ferrari, A. C.; Robertson, J. *Phys. Rev. B* **2000**, *61*, 14095-14107.
9. S. E. Skrabalak, K. S. Suslick, *J. Am. Chem. Soc.* **2006**, *128*, 12642.
10. A. C. Ferrari, J. Robertson, *Phys. Rev. B* **2000**, *61*, 14095.
11. J. Robertson, *Mat. Sci. Eng. R* **2002**, *37*, 129.
12. in CRC Handbook of Physical Constants, 79th ed. (Ed.: D. R. Lide), CRC Press, 1998, pp. 6.
13. C. A. Basar, A. Karagunduz, B. Keskinler, A. Cakici, Appl. Surf. Sci. 2003, 218, 170.
14. S. Paria, C. Manohar, K. C. Khilar, Ind. Eng. Chem. Res. 2005, 44, 3091.
15. S. Paria, K. C. Khilar, Adv. Colloid Interface Sci. 2004, 110, 75.
16. T. F. Tadros, J. Colloid Interface Sci. 1974, 46, 528.
17. Rejman, J.; Oberle, V.; Zuhorn, I. S.; Hoekstra, D. *Biochem. J.* **2004**, *377*, 159-169.
18. Application No: 1091003 through EU laserlab; Characterisation of Mesoporous, and Quantum dot Carbon Particles as Delivery and Imaging agents.

Total internal reflection and single molecule fluorescence microscopy in plant cells

Contact *stephen.webb@stfc.ac.uk*

Gema Vizcay-Barrena

Zoe A. Wilson

School of Biosciences, University of Nottingham, Sutton Bonington Campus, Loughborough, Leicestershire, LE12 5RD, UK

Stephen E. D. Webb

Marisa L. Martin-Fernandez

Central Laser Facility, Science and Technology Facilities Council, Research Complex at Harwell, Rutherford Appleton Laboratory, Didcot, OX11 0QX

Introduction

Determining the distribution of proteins within a cell is critical to understanding their function. The development of fluorescent proteins (FPs) such as GFP and its derivatives has provided scientists with invaluable methods to study the temporal and spatial dynamics of proteins in plants [1]. Combining FPs with the remarkable advances in imaging techniques over the last few decades, it is now possible to visualise and study biological processes at the subcellular level, and even at the single molecule level in a living plant.

Several fluorescence microscopy techniques are available for the study of proteins in living plant cells [2]. In a standard epifluorescence microscope, the sample is wide-field illuminated through the objective and the resultant fluorescence imaged onto a camera or viewed through the eyepiece. However, both in-focus and out-of-focus fluorescent objects contribute signal to the image. The unwanted out-of-focus fluorescence and scattered light contribute high levels of background which must be reduced or eliminated to achieve high levels of contrast and resolution. Various optical sectioning techniques have been developed to achieve this.

One method is Laser Confocal Scanning microscopy (LCSM), which reduces significantly the background caused by out-of-focus and scattered light by inserting a confocal pinhole in front of the detector to spatially filter the fluorescence. This gives a high signal to background ratio and improves the image resolution considerably compared with wide-field fluorescence microscopy, particularly in the axial direction [3]. (The signal to background ratio is a measure of contrast in an image, i.e. the ratio between the intensities of pixels in the focal and deeper planes.) LCSM uses point illumination, which is scanned across the sample to build up an image, which has the disadvantage of requiring long acquisition times and photobleaching of the sample. Image acquisition speeds can be increased using spinning-disk and line-scanning confocal techniques, but there will always be some loss of image resolution.

Total Internal Reflection Fluorescence Microscopy (TIRFM) provides a different route to optical sectioning. When a laser beam strikes the interface between the lens/immersion oil/coverslip and the sample/water at an angle greater than the critical angle (given by Snell's Law), the incident light will undergo total internal reflection because these two groups of materials have different refractive indices. Although the excitation beam does not pass through the sample, an 'evanescent' electromagnetic field is produced whose intensity decays exponentially with distance from the interface into the sample. The field penetrates for a few hundred nanometres (<400nm) into the sample in the *z*-direction [4] and hence only those fluorophores nearest to the glass surface are excited (and their fluorescence collected) by the microscope optics. This limitation on the excitation depth, which could be considered as a disadvantage of this technique, is precisely its main advantage; TIRFM therefore generates images with the highest SBR, where background fluorescence is nearly absent and photobleaching is dramatically reduced. Total internal reflection illumination can be achieved using either a prism-based or, with a high numerical aperture objective lens (NA> 1.4), an objective-based configuration [4].

TIRFM has been widely used to image membrane proteins in animal systems e.g. epidermal growth factor [5], single-channel calcium microdomains [6] and the dynamics of the yeast cytoskeleton [7]. The thinness of the plasma membrane in animal cells makes them ideal for TIRFM. However, its application to plant research has been very limited. Plant cells have a rigid cell wall surrounding the plasma membrane, which varies in thickness depending upon the tissue, growth conditions and developmental stage, but can be greater than 100nm. This thickness could, in principle, prevent the penetration of the evanescent field to the plasma membrane and beyond. The cell wall could also lead to scattering of the illumination resulting in excitation of fluorophores beyond the evanescent field. The consequent view that TIRFM is of limited use with intact plant cells for the visualization of biological processes in and beyond the plasma membrane [2] has caused plant scientists to show little interest in the technique. The few examples include the *in vitro* study of the actin cytoskeleton and microtubule dynamics and ER dynamics in protoplasts, which lack a cell wall [1, 8-10].

By performing a comparative study with other wide-field fluorescence microscopies, we have demonstrated for the first time that TIRFM is a valuable tool for *in vivo* analysis of fluorescent proteins in intact plant cells and can be used for single-molecule analysis in plants. We have shown that TIRF imaging of intact cells is possible, of, for example the plasma membrane and microtubules. We have also described how to distinguish between TIRFM and variable-angle epifluorescence microscopy (VAEM) [11], also known as highly-inclined laminated optical sheet microscopy (HILO [12]), which can be difficult, and demonstrate that the high SBR that we see is indeed due to genuine TIRF. We then demonstrate for the first time in plant cells that TIRFM can be used for single-molecule analysis in plant cells. These techniques, which are becoming routine in mammalian cells, are a major advance for Plant Biology.

TIRF in intact plant cells

We wished to address the use of TIRF in whole plant tissues and determine whether we could image fluorescently labelled proteins in intact cells and in organelles beyond the cell surface. As mentioned previously, there have been major concerns within the scientific community that the plant cell wall would disturb the evanescent field, or simply impede the observation of deeper structures because of its thickness. We therefore imaged intact Arabidopsis roots and were able to detect fluorescence in various subcellular organelles, including microtubules, plasma membrane, vacuolar membrane, endoplasmic reticulum and nuclei, located at the periphery of the intact plant cells due to the presence of the central vacuole. Sample mounting was critical for optimal imaging; ensuring

that the root was touching the bottom of the culture dish was imperative, not only to obtain focussed images, but also to guarantee that the sample to be analysed was within the reach of the evanescent field. In order to be able to compare epifluorescence and TIRF techniques, illumination intensity was kept constant for both illumination modes but the CCD gain was reduced when the epifluorescence images were saturated.

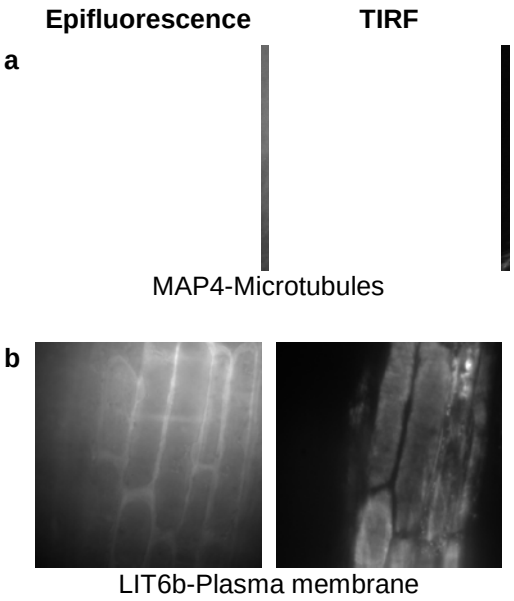

Figure 1*: Epifluorescence (left) and total internal reflection fluorescence (right) microscopy images of plant proteins. The upper panel shows the microtubule marker MAP4-EGFP and the lower panel shows the plasma membrane marker LIT6b-EGFP. Note that the signal to background ratio is much greater with TIRFM, ensuring excellent contrast.*

Figure 1a shows GFP labelled microtubules (MAP4) in the root epidermis. The TIRF image shows a clearer image of the microtubule arrangement, such that individual or small groups of microtubules can be distinguished, with a higher SBR compared with the same cells imaged with epifluorescence illumination.

To visualise localisation within the plasma membrane, we used the marker LTI6b (Figure 1b). While the epi-images showed a blur of fluorescence, the TIRF images provided a more detailed and localised signal, with the detected fluorescence restricted to the plasma membrane of individual cells. It is also evident from these images that TIRF microscopy enhances the visualization of cell structures by removing most of the out-of-focus fluorescence signal. These images revealed a diffuse fluorescence distribution distinct to the LIT6b marker. We can use this specific pattern of expression to infer valuable information about the localization and dynamics of these labelled proteins.

Practical implementation of TIRF in plant microscopy

With variable-angle epifluorescence microscopy (VAEM), the setup is very similar to TIRF microscopy but an evanescent field is not produced because the incident angle is less than the critical angle. A narrow band of illumination passes through the sample almost parallel to the coverslip, yielding a high SBR for visualizing events at, or near the plasma membrane of intact cells. This may allow single molecule imaging in samples where the plane of interest is deeper than the penetration depth of the evanescent field, but at the expense of a higher background signal. In a simple sample, with materials of two refractive indices, it is easy to predict whether the angle at which the beam leaves the objective will result in TIRFM or VAEM. In a plant cell, there may be multiple unquantified refractive indices present, and the microscopy mode is uncertain. However it is only with TIRFM that the excitation beam returns through the objective as an intense reflection, providing an easy method of determining the microscopy mode (Figure 2). (This may not be possible in integrated commercial light-tight microscopes unless they are equipped with a Bertrand lens.) The low divergence and brightness of this returned beam also show that this is not due to scattering by the sample or backreflection from the cover slip.

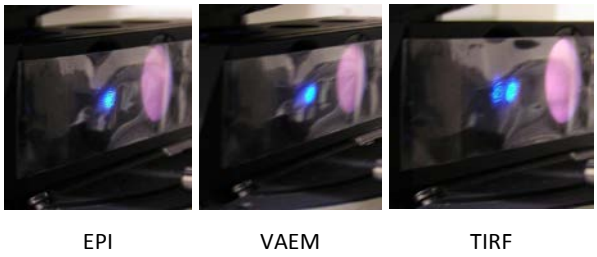

Figure 2*: Identifying whether a sample is being imaged in TIRF or VAEM mode. In TIRFM, the incident beam and reflected beam are both intense. In epifluorescence microscopy, there is no reflected beam apart from some weak reflections coincident beam. With VAEM, these reflections are not coincident but are very weak.*

Single molecule fluorescence microscopy in plant cells

Because TIRFM has a higher signal to background ratio than other fluorescence microscopies, it is possible to perform single molecule fluorescence microscopy studies of plant proteins. Ensemble fluorescence images provide a single measurement from a protein population, hiding rare and asynchronous events. With single molecule detection, however, we can track individual protein molecules in space and time at the same time as determining the stoichiometry of protein clusters.

Single molecule detection requires a very low density of fluorescing molecules, which can be achieved either through using an ultra low initial concentration, or by bleaching a higher concentration. Although the first method is more difficult biochemically with expressed proteins, it may be necessary when the diffusion rate is high enough to maintain a bulk level of fluorescing molecules in the evanescent field.

We demonstrated that single molecule fluorescence microscopy can be carried out in intact plant cells by bleaching MAP4-EGFP. After 75 minutes of epi-illumination, parts of the sample had bleached leaving a low density of individual EGFP molecules which displayed the characteristic blinking of a single molecule.

By collecting a long series of images, it is possible to extract dynamic information on molecules in the sample. Figure 3 shows a typical molecule of MAP4-EGFP through time and space. The intensity and co-ordinates of the molecule were determined for each image in the series, thereby revealing the trace followed by the molecule. This particular molecule displayed a linear back and forth motion, which from observations of the pre-bleached images may coincide with a microtubule.

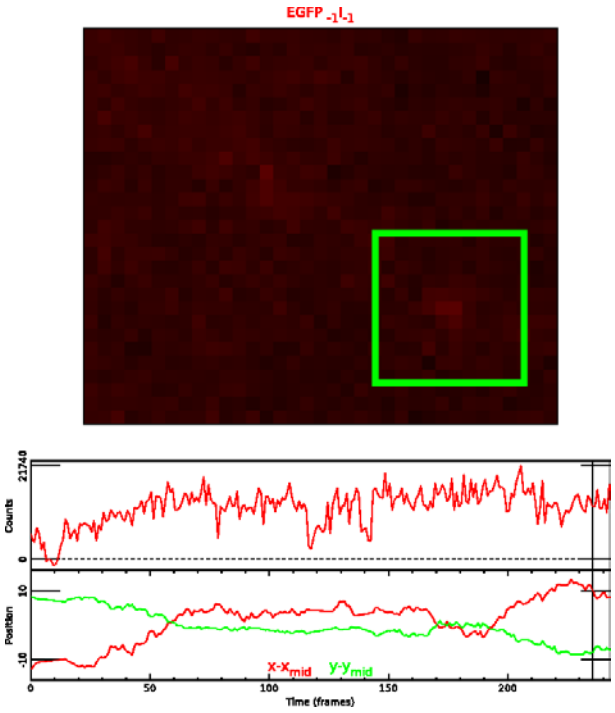

***Figure 3**: Single molecule fluorescence microscopy in plant cells. The fluorescence from a single molecule of MAP4-EGFP is shown within an image at a single time point in the upper panel (within the green square). The fluorescence intensity and x, y position of the molecule over time are shown in the lower panel.*

Conclusions

We demonstrate for the first time that TIRF can be used to generate high contrast images, that are superior to other approaches, from fluorescently labelled proteins in intact plant cells. We also show that TIRF imaging is not only possible at the plasma membrane level, but also in subcellular organelles, for example the nucleus. These TIRF images show the highest signal-to-background ratio and we show that they can be used for single molecule microscopy. This demonstration of the application of TIRFM and single-molecule analysis to plant cells opens up a new range of possibilities for plant cell imaging. This work is currently in press [13].

Acknowledgements

We would like to thank Dr. S. Kurup (Rothamsted Research, Harpenden, UK) for the generous gift of fluorescently labelled marker lines used in this work. We would also like to thank the STFC for providing access to Central Laser Facility and the TIRF microscope and Dr. D. Rolfe for assistance with single molecule data analysis. Financial support was provided by the Biotechnology and Biological Science Research Council and the Science and Technology Facilities Council.

References

1. **Goodin MM, Chakrabarty R, Banerjee R, Yelton S, Debolt S** (2007) New gateways to discovery. Plant Physiol **145:** 1100-1109
2. **Shaw SL** (2006) Imaging the live plant cell. Plant J **45:** 573-598
3. **Conchello JA, Lichtman JW** (2005) Optical sectioning microscopy. Nat Methods **2:** 920-931
4. **Axelrod D** (2001) Total internal reflection fluorescence microscopy in cell biology. Traffic **2:** 764-774
5. **Webb SED, Roberts SK, Needham SR, Tynan CJ, Rolfe DJ, Winn MD, Clarke DT, Barraclough R, Martin-Fernandez ML** (2008) Single molecule imaging and FLIM show different structures for high and low-affinity EGFRs in A431 cells. Biophys. J. **94:** 1-17
6. **Demuro A, Parker I** (2006) Imaging single-channel calcium microdomains. Cell Calcium **40:** 413-422
7. **Chan C, Beltzner CC, Pollard TD** (2009) Cofilin dissociates Arp2/3 complex and branches from actin filaments. Curr Biol **19:** 537-545
8. **Michelot A, Derivery E, Paterski-Boujemaa R, Guerin C, Huang S, Parcy F, Staiger CJ, Blanchoin L** (2006) A novel mechanism for the formation of actin-filament bundles by a nonprocessive formin. Curr Biol **16:** 1924-1930
9. **Vidali L, van Gisbergen PA, Guerin C, Franco P, Li M, Burkart GM, Augustine RC, Blanchoin L, Bezanilla M** (2009) Rapid formin-mediated actin-filament elongation is essential for polarized plant cell growth. Proc Natl Acad Sci U S A **106:** 13341-13346
10. **Ye J, Zheng Y, Yan A, Chen N, Wang Z, Huang S, Yang Z** (2009) Arabidopsis formin3 directs the formation of actin cables and polarized growth in pollen tubes. Plant Cell **21:** 3868-3884
11. **Konopka CA, Bednarek SY** (2008) Variable-angle epifluorescence microscopy: a new way to look at protein dynamics in the plant cell cortex. Plant J **53:** 186-196
12. **Tokunaga M, Imamoto N, Sakata-Sogawa K** (2008) Highly inclined thin illumination enables clear single-molecule imaging in cells. Nat Methods **5:** 159-161
13. **Vizcay-Barrena G, Webb SED, Martin-Fernandez ML, Wilson ZA** (2011) Subcellular and single-molecule imaging of plant fluorescent proteins using total internal reflection fluorescence microscopy (TIRFM). J Exp Bot *in press*

Rapamycin does not affect the interaction between mTOR and raptor but causes increased nuclear levels of highly expressed mTOR in HeLa cells

Contact *rahul.yadav@stfc.ac.uk*

Authors:- R. B. Yadav, C. D. Stubbs, A. W. Parker, S. W. Botchway

Central Laser Facility, STFC, Rutherford Appleton Laboratory, RCaH, Harwell Oxford, OX11FA

V. Iadevaia, C. G. Proud

School of Biological Sciences, University of Southampton, Southampton, SO17 1BJ

Introduction

The mammalian Target of Rapamycin (mTOR) protein kinase is a fundamental regulator of cellular growth, metabolism and proliferation in all eukaryotes (1). mTOR acts as a checkpoint protein regulating functions essential for cell proliferation and survival by acting as a sensor of nutrients and energy availability as well as growth factor receptor activation (Figure 1) (2). mTOR (280 kDa) is a serine/threonine protein kinase belonging to the family of phosphatidylinositol kinase-related kinase (PIKK) as its C-terminal region is homologous to the catalytic domain of phosphatidylinositol 3-kinase (PI3K) (3). The mTOR pathway is activated during various cellular processes (e.g. tumor formation and angiogenesis, insulin resistance, adipogenesis and T-lymphocyte activation) and is deregulated in many human diseases such as cancer and type 2 diabetes. These observations have resulted in broad scientific and clinical interest in the mTOR pathway. The growing use of mTOR inhibitors in pathological conditions, including the treatment of solid tumors, organ transplantation, and rheumatoid arthritis highlighted the importance of mTOR (4).

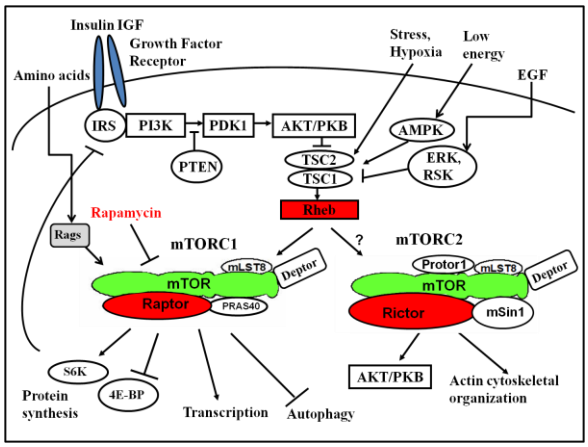

Figure 1. The mTOR signalling pathway in mammalian cells. (modified from (1)).

mTOR was discovered following studies of the mechanism of action of rapamycin (also known as sirolimus), which is a bacterial macrolide that was originally found as an antifungal agent and afterwards recognised as a immunosuppressive and anticancer agent (5). A bacterial strain *Streptomyces hygroscopicus* produces a potent antifungal macrolide which was named rapamycin after Rapa Nui, the place of its discovery. Rapamycin targets a protein suitably named TOR, for target of rapamycin (1).

mTOR forms two distinct functional protein complexes, mTOR complex 1 and mTOR complex 2 referred to as mTORC1 and mTORC2 respectively, on the basis of sensitivity to rapamycin treatment. Some of the functions of the mTORC1 are sensitive to rapamycin inhibition while mTORC2 is insensitive to rapamycin treatment (6, 7).

Rapamycin, upon entering the cell, first complexes with FKBP12 and rapamycin-FKBP12 complex binds to the FRB domain of mTOR and blocks some of the physiological functions of mTORC1. A conserved serine residue, Ser 2035 in FRB domain of mTOR and Ser 1972 in yeast Tor1 is critical for the binding of FKBP12-rapamycin. It interrupts the binding of FKBP12-rapamycin and confers dominant rapamycin resistance when it is mutated to a residue such as threonine (8). The mechanism by which rapamycin inhibits mTOR remains unclear. It is not clear whether rapamycin directly inhibits the intrinsic kinase activity of mTOR, while some reports suggest that FKBP12-rapamycin binding mainly prevents mTOR from interaction with raptor (9). Recent studies have shown that rapamycin inhibits mTOR autophosphorylation (10) which is contrary to an earlier report (11). Cryo-EM studies have proposed that incubation with FKBP12-rapamycin compromises the mTORC1 structural integrity in a stepwise manner (12).

In contrast to mTORC1, the FKBP12-rapamycin complex cannot physically interact with and acutely inhibit mTORC2 (6). However, this hypothesis may not be fully accurate, since chronic treatment of rapamycin, in some cell lines, inhibits mTORC2 activity by blocking its assembly (13). As yet how exactly rapamycin perturbs the function of mTOR is not completely understood. Analogues of rapamycin (CCI-779, RAD001 and AP23573) are likely to be the first mTOR-perturbing molecules to be approved for anticancer use in humans (14).

In the present study we have investigated the localisation of mTOR and its molecular interaction with raptor using highly sensitive Fluorescence Resonance Energy Transfer (FRET) and Fluorescence Lifetime Imaging Microscopy (FLIM) technology in live cells. Effect of rapamycin on the localisation of mTOR and its interaction with raptor was investigated.

Methods

Mammalian Cell culture

HeLa cells (an immortal cell line derived from cervical cancer cells) were cultured in EMEM medium supplemented with 10% FCS, 2 mM L-glutamine, 100 units/ml penicillin G sodium and 100 µg/ml streptomycin and incubated at 37^{o}C with 5% CO_2 in humidified air.

Construction of EGFP-mTOR and mDsRed-Raptor

Enhanced green fluorescent protein (EGFP) was tagged to the N-terminal of mTOR and mDsred tagged at the N-terminal of raptor (15).

Transfection and co-transfection of mammalian cells

For transfection and co-transfection, HeLa cells were plated at 2x10^5 cells/dish, in 35 mm glass bottom dishes (MatTech Corporation, USA). Cells were incubated overnight at 37°C and 5% CO_2 in humidified air prior to the transfection. Cells

were transfected using Fugene HD transfection reagent (Roche Applied Science, UK). For each transfection, DNA and fugene transfection reagent complex was formed by diluting 0.5 µg of plasmid DNA with 100 µl of Opti-MEM I reduced serum medium in polypropylene tubes. Fugene HD transfection reagent (6 µl) was added to the diluted DNA followed by vortexing for 2 s and incubation for 20 min for optimal complex formation. The cell culture medium was replaced with 2 ml of fresh growth medium followed by addition of the transfection complex in a drop-wise manner. Transfected cells were incubated at 37°C and 5% CO_2 humidified air for 24-48 h.

Confocal microscopy and FLIM

Cells expressing fluorescently tagged proteins were viewed using an inverted Nikon Eclipse microscope (TE2000-U) and C1 confocal microscope followed by fluorescence lifetime images acquisition using x60 water, numerical aperture 1.2, objective. An argon ion laser (488 nm) was used to excite the EGFP tagged proteins and green HeNe laser (543 nm) was used to excite mDsRed labelled proteins.

Two-photon induced fluorescence lifetime images were obtained using multiphoton microscopy apparatus built around the above microscope. The multi-photon microscope used in this research was constructed using an external x, y galvanometer scanning system (GSI Lumonics) (16, 17). The set up consisting of a high-powered titanium sapphire (Ti:Sa) laser (MIRA 900, Coherent Lasers) tuneable between 680–1100 nm. The Ti:Sa laser itself was pumped using a solid-state Neodynium:Vanadate laser (Verdi V18, Coherent Lasers). Laser light at a wavelength of 910 ± 5 nm was obtained from Ti:Sa laser with 180 fs pulse width at 75 MHz. The nominal laser power at the microscope stage was adjusted to 0.60-0.130 mW using a neutral density filter for excited state lifetime measurement of the donor EGFP.

TCSPC lifetime imaging micrographs were analysed using the SPCImage 2.92 analysis software (Becker and Hickl, Germany). Images (128×128 pixel or 256×256 pixel) were exported from Becker & Hickl software as bitmaps and converted into TIFF files. The optimal curve fitting for the decay graph was obtained by varying different parameters. An exponential decay fit was considered good when the $\chi 2$ value was near 1.

Results and discussion

Rapamycin causes increased nuclear levels of highly expressed mTOR in HeLa cells

It has been reported earlier that rapamycin treatment does not show any effect on the localisation of mTOR (18). In this study the effect of rapamycin on the localisation of mTOR and raptor was investigated in live cells. HeLa cells transfected with EGFP-mTOR vector were treated with 100 nM rapamycin for 24 h and imaged using confocal microscopy and FLIM. Surprisingly, it was observed that EGFP-mTOR levels within the nucleus increased following incubation with rapamycin (Figure 2) when compared to non-treated cells. Around 5-6 % of cells showed a change in localisation pattern following rapamycin treatment in HeLa cells expressing EGFP-mTOR. On the other hand, the localisation of mDsRed-raptor was not affected by rapamycin treatment (Figure 3).

The change in the localisation of fluorescently tagged mTOR upon rapamycin treatment i.e. to a nuclear localisation, was in agreement with cell fractionation data performed using HeLa cells by Dr. Valentina Iadevaia (personal communication). This data is contrary to that described for the same cell line (18) and cell fractionation data for non-transformed, non-immortalised, diploid human primary fibroblasts, IMR-90 cells (19). In the present study, fluorescently tagged mTOR was overexpressed in HeLa cells while in the previous study endogenous mTOR expression was studied using immunofluorescence assay (18). Although the frequency of cells observed with nuclear localisation is low (less than 10% of the field of view).

It has been previously reported that a moderate increase in mTOR nuclear import enhances 5'-TOP dependent translation and a strong nuclear import signal causes decrease in translation (20). It was further suggested that nuclear shuttling of mTOR is essential for the regulation of rapamycin-sensitive translation initiation. Nuclear import and subsequent export of mTOR would be required for its function, optimal balance between the two events leading to maximal activation. A moderate increase in the nuclear import of mTOR may result in the perfect balance, whereas an increased nuclear localisation signal may disrupt that balance (20). Thus, in the present study rapamycin treatment may disturb the balance between nuclear import and export of mTOR, since greater mTOR levels in the nucleus may affect the translation as described by Kim *et al* (20). Long term treatment of rapamycin causes hyperphosphorylation of 4E-BP1 (21), thus, another possibility could be that increased nuclear mTOR causes hyperphosphorylation of 4E-BP1. However, the microscopy image data show only a small fraction of cells expressing a nuclear localisation of mTOR. So this effect may depend on the state of the cell cycle or other factors and further work is needed to clarify this issue.

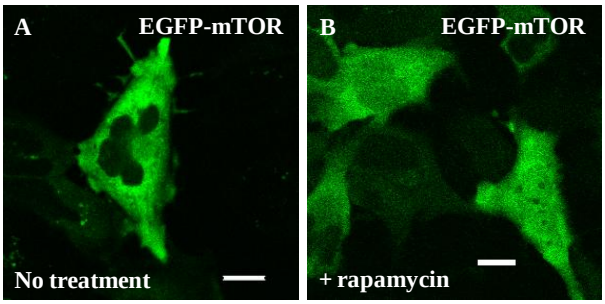

Figure 2. Rapamycin treatment affects the localisation of EGFP-mTOR in HeLa cells. Confocal images of HeLa cells expressing EGFP-mTOR A) no treatment and B) rapamycin (100 nM) treatment for 24 h. Data were obtained from three independent experiments. Scale bar 8 µm.

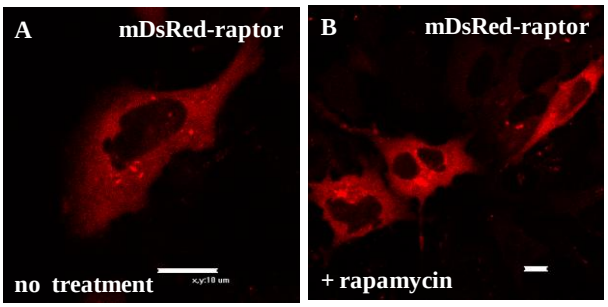

Figure 3. Rapamycin treatment does not affect the localisation of mDsRed-raptor in HeLa cells. Confocal images of HeLa cells expressing mDsRed-raptor A) no treatment and B) rapamycin (100 nM) treatment for 24 h. Data were obtained from three independent experiments. Scale bar 8 µm for B.

Rapamycin does not affect the interaction between mTOR and raptor

To investigate whether the change in localisation of EGFP-mTOR following rapamycin treatment was associated with any effect on the interaction between mTOR and raptor, HeLa cells were co-transfected with EGFP-mTOR and

mDsRed-raptor vectors. Cells were treated with rapamycin (100 nM) for 24 h and analysed using confocal microscopy and FLIM. The lifetime of the cells showing nuclear localisation of EGFP-mTOR observed to be ~2.2 ± 0.1 ns, showing a direct interaction (Figure 4). The quenched lifetime value is similar to the non-treated HeLa cells (~2.2 ± 0.1 ns), co-expressing EGFP-mTOR and mDsRed-raptor (data not shown). There was no effect on the lifetime of EGFP attached to mTOR as a result of rapamycin treatment (Figure 4).

The FLIM data indicate that mTOR pathway inhibitor rapamycin does not dissociate the interaction of co-expressed mTOR and raptor. There may be different mechanisms for the action of rapamycin, other than dissociation of mTOR-raptor interaction. It was reported earlier that rapamycin dissociates the mTOR-raptor interaction (9) while Hara *et al* (22) did not observe dissociation after rapamycin treatment. In the present study, rapamycin treatment did not affect the interaction between fluorescently tagged mTOR and raptor in HeLa cells supporting the observations of Hara *et al* (22). It is clear from our studies that rapamycin treatment increases the nuclear localisation in HeLa cells.

Rapamycin-FKBP12 binding to the FRB domain of mTOR induces an allosteric conformational change that reduces mTORC1's intrinsic catalytic activity (10). The present interaction data after rapamycin treatment suggests that there could be conformational changes in mTORC1 after rapamycin treatment but that may not lead to changes in the direct interaction between mTOR and raptor but that nevertheless act to reduce intrinsic mTOR catalytic activity. Rapamycin inhibition of mTORC1 may indeed involve more than one mechanism. Any conformational changes in mTORC1 following rapamycin treatment may lead to changes in the interaction between mTOR and its substrates (11, 23) or could theoretically hinder reception of an upstream activating signal or impair access of docked substrates to the mTOR catalytic domain (11) or in addition to, inhibition of intrinsic mTOR kinase activity (6, 10).

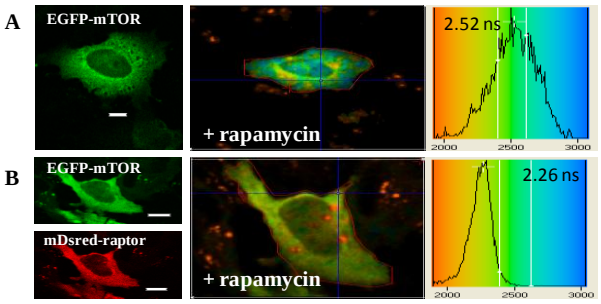

Figure 4 Rapamycin does not affect the direct interaction between EGFP-mTOR and mDsRed-raptor in HeLa cells. A) A Lifetime image (middle panel) of the HeLa cell expressing EGFP-mTOR treated with rapamycin (100 nM) for 24 h, with confocal image (left panel) at 488 nm excitation for EGFP-mTOR donor and colour coding of the analysis area (right panel) gave an average lifetime of ~2.4 ± 0.1 ns. B) A Lifetime image (middle panel) of HeLa cells co-expressing EGFP-mTOR and mDsRed-raptor treated with rapamycin 100 nM for 24 h, with confocal images (left panel) at 488 nm excitation for EGFP-mTOR donor and 543 nm excitation for mDsRed-raptor acceptor and colour coding of the analysis area (right panel) giving an average lifetime of ~2.2 ± 0.1 ns. Data were obtained from three independent experiments. Scale bar 8 µm.

Conclusions

A small fraction of HeLa cells showed an increased level of nuclear localisation of EGFP-mTOR following treatment by rapamycin. Using FLIM-FRET no change in the interaction between mTOR and raptor was observed suggesting that rapamycin does not act by dissociating the mTORC1 complex.

Acknowledgements

We thanks Biomed network, STFC and UCB-Pharma for funding.

References

1. Wullschleger S, Loewith R, Hall MN. TOR signaling in growth and metabolism. Cell 2006;124(3):471-484.

2. Lane HA, Breuleux M. Optimal targeting of the mTORC1 kinase in human cancer. Current opinion in cell biology 2009;21(2):219-229.

3. Sabatini DM, Erdjument-Bromage H, Lui M, Tempst P, Snyder SH. RAFT1: a mammalian protein that binds to FKBP12 in a rapamycin-dependent fashion and is homologous to yeast TORs. Cell 1994;78(1):35-43.

4. Laplante M, Sabatini DM. mTOR signaling at a glance. Journal of cell science 2009;122(Pt 20):3589-3594.

5. Sabatini DM. mTOR and cancer: insights into a complex relationship. Nature reviews 2006;6(9):729-734.

6. Jacinto E, Loewith R, Schmidt A, Lin S, Ruegg MA, Hall A, Hall MN. Mammalian TOR complex 2 controls the actin cytoskeleton and is rapamycin insensitive. Nat Cell Biol 2004;6(11):1122-1128.

7. Sarbassov DD, Ali SM, Kim DH, Guertin DA, Latek RR, Erdjument-Bromage H, Tempst P, Sabatini DM. Rictor, a novel binding partner of mTOR, defines a rapamycin-insensitive and raptor-independent pathway that regulates the cytoskeleton. Curr Biol 2004;14(14):1296-1302.

8. Brown EJ, Beal PA, Keith CT, Chen J, Shin TB, Schreiber SL. Control of p70 s6 kinase by kinase activity of FRAP in vivo. Nature 1995;377(6548):441-446.

9. Oshiro N, Yoshino K, Hidayat S, Tokunaga C, Hara K, Eguchi S, Avruch J, Yonezawa K. Dissociation of raptor from mTOR is a mechanism of rapamycin-induced inhibition of mTOR function. Genes Cells 2004;9(4):359-366.

10. Soliman GA, Acosta-Jaquez HA, Dunlop EA, Ekim B, Maj NE, Tee AR, Fingar DC. mTOR Ser-2481 autophosphorylation monitors mTORC-specific catalytic activity and clarifies rapamycin mechanism of action. The Journal of biological chemistry 2010;285(11):7866-7879.

11. Peterson RT, Beal PA, Comb MJ, Schreiber SL. FKBP12-rapamycin-associated protein (FRAP) autophosphorylates at serine 2481 under translationally repressive conditions. The Journal of biological chemistry 2000;275(10):7416-7423.

12. Yip CK, Murata K, Walz T, Sabatini DM, Kang SA. Structure of the human mTOR complex I and its implications for rapamycin inhibition. Molecular cell 2010;38(5):768-774.

13. Sarbassov DD, Ali SM, Sengupta S, Sheen JH, Hsu PP, Bagley AF, Markhard AL, Sabatini DM. Prolonged rapamycin treatment inhibits mTORC2 assembly and Akt/PKB. Molecular cell 2006;22(2):159-168.

14. Guertin DA, Sabatini DM. An expanding role for mTOR in cancer. Trends in molecular medicine 2005;11(8):353-361.

15. Yadav R. Studies of the mTOR Signalling Pathway using an Advanced FRET-FLIM Technique. PhD Thesis 2011.

16. Stubbs CD, Botchway SW, Slater SJ, Parker AW. The use of time-resolved fluorescence imaging in the study of protein kinase C localisation in cells. BMC Cell Biol 2005;6(1):22.

17. Botchway SW, Barba I, Jordan R, Harmston R, Haggie PM, Williams SP, Fulton AM, Parker AW, Brindle KM. A novel method

for observing proteins in vivo using a small fluorescent label and multiphoton imaging. The Biochemical journal 2005;390(Pt 3):787-790.

18. Drenan RM, Liu X, Bertram PG, Zheng XF. FKBP12-rapamycin-associated protein or mammalian target of rapamycin (FRAP/mTOR) localization in the endoplasmic reticulum and the Golgi apparatus. The Journal of biological chemistry 2004;279(1):772-778.

19. Rosner M, Hengstschlager M. Cytoplasmic and nuclear distribution of the protein complexes mTORC1 and mTORC2: rapamycin triggers dephosphorylation and delocalization of the mTORC2 components rictor and sin1. Hum Mol Genet 2008;17(19):2934-2948.

20. Kim JE, Chen J. Cytoplasmic-nuclear shuttling of FKBP12-rapamycin-associated protein is involved in rapamycin-sensitive signaling and translation initiation. Proceedings of the National Academy of Sciences of the United States of America 2000;97(26):14340-14345.

21. Choo AY, Yoon SO, Kim SG, Roux PP, Blenis J. Rapamycin differentially inhibits S6Ks and 4E-BP1 to mediate cell-type-specific repression of mRNA translation. Proceedings of the National Academy of Sciences of the United States of America 2008;105(45):17414-17419.

22. Hara K, Maruki Y, Long X, Yoshino K, Oshiro N, Hidayat S, Tokunaga C, Avruch J, Yonezawa K. Raptor, a binding partner of target of rapamycin (TOR), mediates TOR action. Cell 2002;110(2):177-189.

23. Nojima H, Tokunaga C, Eguchi S, Oshiro N, Hidayat S, Yoshino K, Hara K, Tanaka N, Avruch J, Yonezawa K. The mammalian target of rapamycin (mTOR) partner, raptor, binds the mTOR substrates p70 S6 kinase and 4E-BP1 through their TOR signaling (TOS) motif. The Journal of biological chemistry 2003;278(18):15461-15464.